Utrecht University

MSc Thesis – Earth Structure and Dynamics

Time-dependent frictional healing mechanisms of smectite-rich clay gouge

Erik Giliam, 6167144

Supervisors:

Dr. André Niemeijer

Mike Sep

May 2024

Abstract

Over the last decades, significant induced seismicity has been experienced in the Groningen gas field in the North-East of the Netherlands (Buijze et al., 2019; Dost et al., 2012). Pre-existing faults that run through the sandstone reservoir into the adjacent formations are reactivated because of changing conditions in the subsurface due to gas production (Van Eijs et al., 2006). This seismic activity is dependent on the strength of the material which is controlled by the healing during an interseismic period. Frictional healing during the seismic cycle has been found to be necessary for repeated earthquake failure of faults (Marone and Saffer 2015). It is therefore essential to understand the mechanisms responsible for fault healing in order to model and predict the behaviour of induced seismicity. A lot of research has been done on calcite, feldspar and quartz-rich gouge material (Karner & Marone, 1998; Niemeijer et al., 2008; Tao & Dang, 2023; Verberne et al., 2014), but the healing mechanisms of clay-rich formations is less understood. Therefore, the aim of this study is to add to the understanding of time-dependent healing mechanisms of clay-rich fault gouge by performing frictional experiments in a hydrothermal ring shear apparatus to investigate the mechanical properties of smectite-rich gouge. Slide-hold-slide experiments were performed in a ring shear in order to study the time-dependent healing behaviour of Opalinus claystone and smectite rich gouge (SWy-2). The results showed contrasting behaviour between the two materials. Opalinus claystone did exhibit minimal frictional healing ($\Delta\mu < 0.005$) in the time-scale of the laboratory experiments of this study ($<3 \times 10^4$ s after seismic activity), while smectite-rich gouge demonstrated significant healing ($\Delta\mu$ up to 0.05) with frictional strengthening rates of 1.25 to 12.53 x 10^{-3} log(s^{-1}). This study revealed a positive correlation of the amount and rate of healing with temperature and pore fluid pressure and a negative correlation with the effective normal stress. Higher temperatures, pore fluid pressures and lower effective normal stress facilitate the ease in which water is able to enter the interlayer spaces of the smectite minerals. Water sorption consequently leads to swelling of the material (Zhang 2019), suggesting that sorption is the dominant healing mechanism of clay-rich fault gouge containing smectite. Additionally, this study revealed that the rate-and-state velocity dependence of smectite changes not only with varying conditions but also with the length of the hold time. This means that an increased temperature has a negative effect on the velocity-strengthening behaviour after more than 1 x 10^2 s after seismic activity, while the pore fluid pressure promotes the velocity-strengthening behaviour in the timescale up to 1 x 10^4 s. These findings suggest that the presence of smectite in the clay-rich layers adjacent to the Groningen gas field result in reduced frictional healing due to decreasing pore fluid pressure and increasing effective normal stress. However, these conditions also lead to less velocity-strengthening behaviour, thereby increasing the chance of earthquake propagation into the adjacent clay-rich layers of the gas field.

Introduction

The strength evolution of faults during the seismic cycle plays a crucial role in the behaviour of earthquakes (Carpenter et al., 2016; Hillers et al., 2009; McLaskey et al., 2012). Between seismic events, faults restrengthen through a combination of physical and chemical healing processes. Without restrengthening, a fault is not able to undergo repeated earthquake failure meaning the frictional failure and frictional strength of a fault are closely interconnected (Marone and Saffer 2015). Understanding the healing processes of a fault is therefore essential for determining the size and recurrence of earthquakes (McLaskey et al., 2012). Previous studies determined that the following parameters significantly affect the strength and stability of faults: grain size, roughness and distribution of the gouge, mineralogy, porosity, temperature, effective normal stress, pore fluid pressure, slip velocity and slip distance (Moore and Lockner 2007; Marone and Saffer 2015).

It is important to understand how these parameters influence the healing process of a particular fault zone which is key for determining the slip behaviour and stability of different formations. This is particularly important for regions which experience induced seismicity due to natural oil and gas recovery, geothermal energy production, or other industries which influence the conditions of the subsurface. A substantial amount of induced seismicity has been observed in the Groningen gas field in the North-East of the Netherlands due to the reactivation of pre-existing normal faults as the result of gas production (Buijze et al., 2019; Dost et al., 2012). These pre-existing faults run through the sandstone reservoir into the adjacent layers (Van Eijs et al., 2006). To accurately model and predict the behaviour of induced seismicity in the Groningen gas field, it is crucial to understand the healing mechanisms and the effects of previously described parameters on the strength evolution and thus healing behaviour of the gouge materials found in the formations of Groningen gas field.

The Basal Zechstein caprock of the Groningen gas field consists primarily of anhydrite and carbonates, the Ten Boer claystone predominantly of quartz and phyllosilicates and the underlying Carboniferous formation of quartz and phyllosilicates (Hunfeld et al., 2020). Previous studies found that the strength and rate of healing strongly depend on the mineralogy of the fault zone (Byerlee, 1978; Carpenter et al., 2016; Saffer & Marone, 2003). Phyllosilicate-rich gouges are known for the lowest frictional healing rates, while feldspar and quartz-rich gouges have intermediate healing rates, and calcite-rich gouges exhibit the largest healing rates (Carpenter et al., 2016). This is in line with the observed healing behaviours in the different formations of the Groningen gas field. The Basal Zechstein shows significantly more healing and frictional strength compared to the phyllosilicate-rich Ten Boer and Carboniferous formations. As a result, these phyllosilicate-rich formations tend to have a lower potential for seismic activity (Hunfeld et al., 2020).

The healing behaviour of quartz- and calcite-rich fault gouge has been extensively studied (Karner & Marone, 1998; Smith et al., 2015; Tao & Dang, 2023) but the effect of swelling clays alone on frictional healing is less well understood. Studies on phyllosilicates in combination with other minerals revealed that phyllosilicate minerals can reduce frictional healing (Carpenter et al., 2016; Seyler et al., 2023). Although some research has reported on the healing of smectite-rich faults, these studies only report on the healing in combination with other minerals. Consequently, there has been no systematic studies on the effect of temperature, effective normal stress or pore fluid pressure solely on smectite. This information is crucial for identifying the specific healing mechanisms responsible for healing in smectite-rich clay

gouges. Therefore, this study aims to enhance our understanding of time-dependent healing mechanisms of clays-rich fault gouge, with a particular focus on smectite.

This is achieved by performing frictional experiments in a hydrothermal ring shear (RS) apparatus to study the mechanical properties of smectite-rich gouge. The effect of different conditions on the frictional healing of smectite-rich clays were studied with slide-hold-slide (SHS) experiments in the RS. SHS tests were conducted to investigate the time-dependent healing behaviour and further rate-and-state friction analysis on the data. Understanding the behaviour of smectite-rich clays under these conditions provides valuable information for regions such as the Groningen gas field, where subsurface stability is affected by gas production, and for other regions where the conditions are changed due to geothermal exploration.

Background

Mechanical properties and shear strength of specific materials can be researched with SHS experiments in for example a RS apparatus. Most SHS experiments are performed under constant normal stress, temperature, pore fluid pressure and constant shearing rates. During the SHS experiments, parameters such as the steady state friction (μ_{ss}), frictional healing ($\Delta\mu$) and creep relaxation ($\Delta\mu_c$) can be measured. The steady state friction is defined as the condition where a material exhibits continuous movement while maintaining a constant friction value. This occurs when the system has reached a balance between driving forces and resistance due to friction, resulting in a stable, unchanging friction coefficient during ongoing sliding (Marone and Saffer 2015). In the SHS sequence, hold periods are programmed to occur when the material is in steady-state sliding. A hold period begins when the initial velocity is switched to zero and ends when the initial velocity is resumed. Immediately after the onset of the hold period, frictional creep relaxation initiates, following a logarithmic decay curve over time until sliding is resumed. Due to the finite stiffness of the apparatus, the fault surface velocity will never reach zero (Rabinowicz, 1956). The total decrease in frictional force during the hold defines the creep relaxation (Marone and Saffer 2015). During this hold period, the material regains strength though frictional healing processes, which results in a peak friction upon re-sliding (Marone and Saffer 2015).

During the late 1970s and early 1980s, Dieterich (1979) and Ruina (1983) introduced a series of empirical friction or shear stress equations designed to capture detailed experimental outcomes, particularly capturing the transient friction response following a quasi-instantaneous change in load-point velocity. These equations are named the Rate-and-State Friction (RSF) equations and can be used to fit experimental data:

$$\mu(V,\theta) = \mu_0 + aln\left(\frac{V}{V_0}\right) + bln\left(\frac{V_0\theta}{d_c}\right) \quad (1)$$

In this equation, μ is the reference coefficient of friction at sliding velocity V_0. a and b are thought to represent material properties, where a quantifies the "direct" effect and b describes the "evolutionary" effect. d_c describes the characteristic or critical slip distance over which the new variable θ evolves. This gives θ the unit of time and represents the grain-scale asperity contact lifetime which can be formulated by the "ageing law" (Dieterich 1979):

$$\frac{d\theta}{dt} = 1 - \frac{\theta V}{d_c} \quad (2)$$

or "slip law" (Ruina, 1983):

$$\frac{d\theta}{dt} = \frac{V\theta}{d_c}\ln\left(\frac{V\theta}{d_c}\right) \quad (3)$$

The concept of the RSF originates from two fundamental observations: firstly, that the actual contact area of any interface is constantly smaller than the nominal contact area and secondly, that this contact area changes over time. Two different evolution equation created by Dieterich (1979) and Ruina (1983), offer two distinct perspectives on how a population of contacts evolve. Equation 2, created by Dieterich (1979), also referred to as the slowness or aging law because it describes how the frictional contact evolves in the absence of slip. This model suggests that the state variable, representing the contact area and its strength, increases over time when there is no relative motion between the surfaces. In contrast, equation by Ruina (1983) proposes that

slip is necessary for the state variable to evolve, indicating that the evolution of friction is directly tied to sliding activity (Marone and Saffer 2015).

The *a-b* parameter is crucial in studies on crustal faults because it determines the potential for sliding instabilities to nucleate, which can result in earthquake rupture. A positive *a-b* value indicates velocity-strengthening behaviour, where friction increases with sliding and consequently stabilizing the sliding behaviour. In contrary, a negative *a-b* value indicates velocity-weakening behaviour, leading to unstable sliding and potential earthquake rupture (Marone and Saffer 2015).

Smectite Sorption

Different types of phyllosilicates demonstrate varying degrees of volumetric changes when exposed to water. Smectite $(Na,Ca)_{0.33}(Al,Mg)_2(Si_4O_{10})(OH)_2$ is a phyllosilicate known for its high swelling potential and will undergo significant volumetric changes when it is exposed to water (Di Maio et al., 2004; Saiyouri et al., 2004). The smectite clay minerals are layered with a 2:1 structure consisting of an AL-O octahedral central sheet (O) that is sandwiched between two negatively charged Si-O tetrahedral sheets (T), forming a TOT structure (Figure 1) (Zhang 2019). The negative charge on the silicate sheets allows for multivalent cations such as Na^+, K^+ and Ca^{2+} to be incorporated into the interlayer regions to balance the negative charge (Zhang 2019). Subsequently, these cations attract water molecules to the interlayer regions which results in swelling of the lattice normal to the sheet layers (Figure 1B) (Morodome & Kawamura, 2009; Saiyouri et al., 2004).

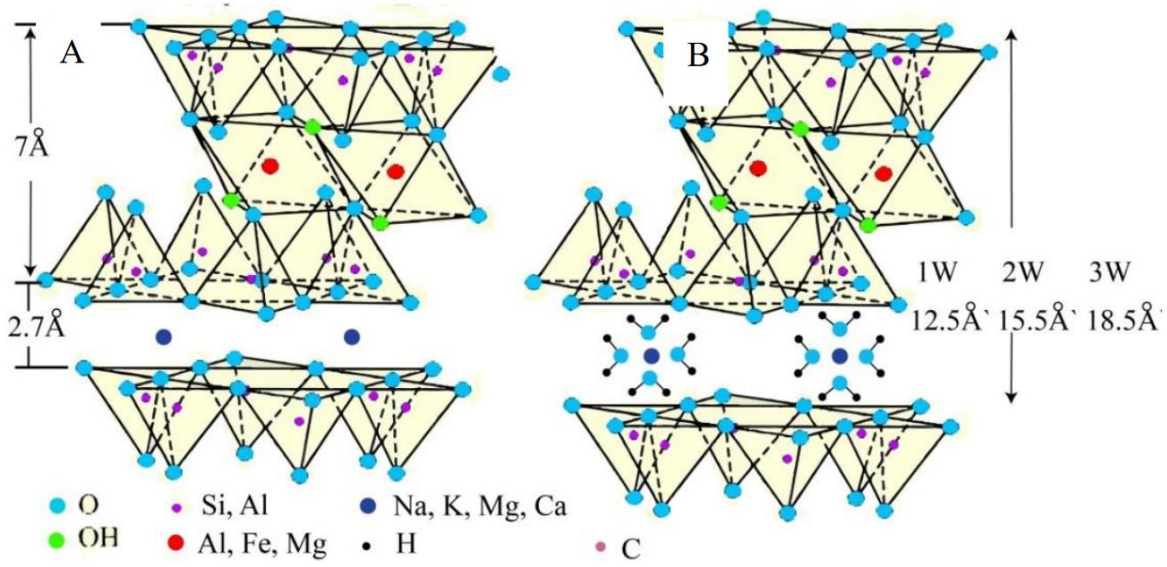

Figure 1: Schematic crystal structure of smectite clay made up of octahedral and tetrahedral sheets. a) interlayer cations balance the negatively charged layers or b) balanced by water incorporated into the interlayer which results in swelling of the structure dependent on the amount of water layers. From Zhang (2019).

The layered structure of smectite and other phyllosilicates results in the individual layers being significantly stronger than the interlayer bonds, leading to a perfect cleavage parallel to the (001) plane. This shape anisotropy significantly affects the frictional properties and strength of phyllosilicate minerals (Moore & Lockner, 2007). Dry smectite gouge undergoes normal frictional processes such as wear, abrasion, and fracture during shearing. However, the frictional behaviour changes significantly when the material is saturated with water (Morrow et al. 2017). A thin water film absorbs on the (001) plane of the smectite, concentrating shear

along this plane and causing relative weakness in water-saturated smectite (Moore and Lockner 2007). This saturation of the contact area is thought to result in slow strength recovery after failure (Tesei et al., 2012), and the strength of the water bonds seem to directly control the strength of the clay gouge (Moore and Lockner 2004). Contrary, the water bonds can also strengthen the material because these bonds are stronger than the interlayer bonds of the phyllosilicates. An increased surface charge will strengthen the bonded water films, leading to a higher coefficient of friction (Moore and Lockner 2007).

Seyler et al. (2023) found (with SHS experiments on a gouge mixture of wet smectite and quarts) that the rate and magnitude of healing decrease, if the smectite content is increased until approximately 80% smectite. In addition, the frictional healing scales with two things. Firstly, with layer-normal compaction of the gouge and secondly with the creep relaxation during the holds. This suggests that the alignment of clay minerals leads to saturation of the contact area which limits the restrengthening of clay-rich fault gouge during hold periods (Seyler et al., 2023). The amount of swelling is dependent on the hydration state which is influenced by different conditions such as the temperature and effective normal stress (Zhang 2019).

The temperature has various effects on different processes inside the clay. For example, with an increase in temperature, the kinetic energy of water also increases which affects the interaction with the clay minerals. The increased energy makes the water less uniform an enhances the ability to penetrate into the interlayer spaces, leading to increased hydration and swelling of the clay (Saiyouri et al., 2004). Additionally, the mineral lattice of the clay undergoes thermal expansion after heating, contributing to increased interlayer spacing and swelling (Chorom & Rengasamy, 1996). Di Maio et al. (2004) studied the influence of the stress level on the swelling behaviour of artificial mixtures and natural soils containing smectite. These authors found that increasing axial stress reduces the compressibility and swelling capacity of the clay. Furthermore, they found that the effect of the pore fluid pressure on the swelling ability of clay makes the material less compressible which leads to an increase in clay swelling (Di Maio et al., 2004).

Morrow et al. (2017) found that the frictional strength of smectite of wet smectite depends on the saturation state. They noted that a wide range of frictional strength values reported in literature can be attributed to various experimental procedures. These dissimilar procedures leads to different degrees of partial saturation or pore fluid conditions that are overpressured. In particularly saturated samples, the amount of adsorbed water significantly influences frictional strength by acting as a lubricant on the clay platelets (Moore and Lockner 2007). Overpressure occurs when the strain rate is too rapid, trapping water in pores and leading to overpressure within those pores (Morrow et al. 2017). It is therefore important not to shear the sample too quickly in experiments on saturated smectite.

The temperature seems to have a positive effect on the strength of smectite. The study from Boulton et al. (2014) compared smectite-rich clay to illite/muscovite and found that smectite is approximately 30% weaker at room temperature while being stronger above 140 °C. The effect of temperature on frictional healing was also studied by Shibasaki et al. (2017) and they found that the amount of frictional healing increases with temperature. Other studies investigated the effect of effective normal tress on the frictional strength and healing. Different effects were found with both increasing (Morrow et al. 2017) and decreasing (Mizutani et al., 2017) effects of the effective normal stress on the steady state friction.

Method

Sample material

In this study, experiments were performed on three different batches of Opalinus claystone (OPA) along with experiments on smectite (SWy-2). The Opalinus batches have a similar composition to the clay-rich layers found directly above and below the Groningen gas field but differ in concentrations of smectite. These three batches were compared to “pure” smectite to study the effects of swelling clays on the frictional healing of clay-rich fault gouge.

The Opalinus batch 1 (OPA1) in this study was provided from experiments conducted by (Bakker, 2017). A mean value from multiple batches of Opalinus analyse by Bakker and De Bresser (2020) indicate that the material consist of 47% phyllosilicates, 26% calcite, 23% quartz and 4% pyrite. OPA1 was labelled as “Opalinus batch 4” in the experiments of Bakker (2017). The second Opalinus batch (OPA2) in this study was also used in experiments from Elisenda Bakker and indicated with “chunks remaining from a coarse fraction” on the sample container. The third Opalinus batch (OPA3) comes from a cylindrical Opalinus sample labelled with "V8". The mineral composition of Opalinus claystone drilled by Mont Terri Underground Rock Laboratory has a composition of approximately 65% clay particles. These claystone consist mainly of kaolinite and illite with only 10% comprising of a mixture of illite-smectite layers. The other 35% comprises of quartz, calcite and feldspar (Corkum & Martin, 2007). The smectite clay material used in this study originates from "The Clay Mineral Society's" Source Clays Repository and contains sodium-rich montmorillonite from Cook County, Wyoming, USA (The Clay Minerals Society, n.d.).

To achieve a uniform grain size representative of fault gouge, the Opalinus claystone material was initially crushed with a pestle and mortar, followed by sieving though a 75 µm sieve. If not all the material passed through the sieve, the remaining chunks were further crushed and sieved until the material met the specified grain size. For the OPA3 batch, a chunk of the V8 Opalinus sample was initially gently coarsely disaggregated with a hammer and subsequently processed similar to the other OPA batches.

Thermogravimetric Analysis (TGA) was performed on the samples in order to estimate the relative smectite content of the three different OPA batches. This technique measures the change in mass as a function of temperature by heating up material. In this study, the TGA 2950 from the Earth Simulation Lab of the University of Utrecht has been used. About 25 mg of OPA or SWy-2 was deposited on a small tray that is picked up by a hook in the machine. This hook is connected to a scale for weight measurement. During the analysis, material was heated to 900 °C with a ramp of 10 °C/min. Nitrogen gas was used as the cooling gas after the measurement. Using the software TA Universal Analysis, the weight loss at specific temperature intervals was measured. This gives an indication for the relative smectite content compared to the other batches. Information about the changes in mass can be used for identification and quantification of the composition of the material by matching the data with thermal decomposition curves of specific minerals (Földvári, 2011). Additionally, a duplicate analysis was performed on every batch to verify the reproducibility of the TGA results.

The particle size distribution of SWy-2 was measured with the particle size analyser of the Earth Simulation Lab of the University of Utrecht. Gouge material was initially mixed with demineralized water to form a suspension. Due to clumping of the material during the RS experiment, chunks were firstly disaggregated with a pestle and mortar. Subsequently, an ultrasonic bath was used to get the material fully into suspension. The analysis procedure

started with first calibrating the medium without added material. Suspension was carefully added to the QS sample presentation unit with a pipet until an obscuration percentage of approximately 11% was reached. Subsequently, the particle size distribution was measured by the apparatus which uses a laser to obtain the scattering and intensity. Because SWy-2 has a refractive index of 1.48 to 1.64, the 3OHD (non-transparent) presentation method was used in this study. This procedure was repeated three times for every sample in order to validate the reproducibility.

Ring shear apparatus

The hydrothermal RS apparatus (Figure 2), designed and built at the HPT laboratory of the University of Utrecht previously described by Niemeijer et al. (2008), was used to perform the SHS experiments in this study. The sample-piston assembly is housed in a water-cooled pressure vessel that is capable of reaching high pressure and temperature conditions (fluid pressures up to 300 MPa and temperatures of 700 °C) (Figure 2b). This vessel is positioned within an Instron servo-controlled loading frame, which can apply an axial load to the sample assembly through a pressure-compensated piston (up to 300 MPa). The applied effective normal stress is externally measured using a 100 kN axial load cell and is maintained constant within approximately 0.05 MPa using the load control function of the Instron menu.

Demineralized water serves as the pore fluid phase with direct access to the sample. The applied pore fluid pressure is measured with a resolution of 0.015 MPa. The pore fluid phase and sample can be heated internally using a furnace element, with temperature monitored by two thermocouples with an accuracy of approximately 0.1 °C. One thermocouple is located near the sample close to the furnace element, the other is connected to the bottom piston with a kanthal wire that wraps around the piston. Vertical displacement of the leading piston relative to the pressure vessel is accurately measured using an externally located LVDT, with the Instron ram offering a resolution of 0.005 mm. On the lower Instron loading ram, a motor and gearbox system rotates the vessel and subsequently the lower piston to impose shear on the sample. Displacement is measured using a geared potentiometer that has a resolution of 0.001 mm. The top part of the piston is fixed and connected to a torque bar equipped with two load cells at the end, which measure the shear stress.

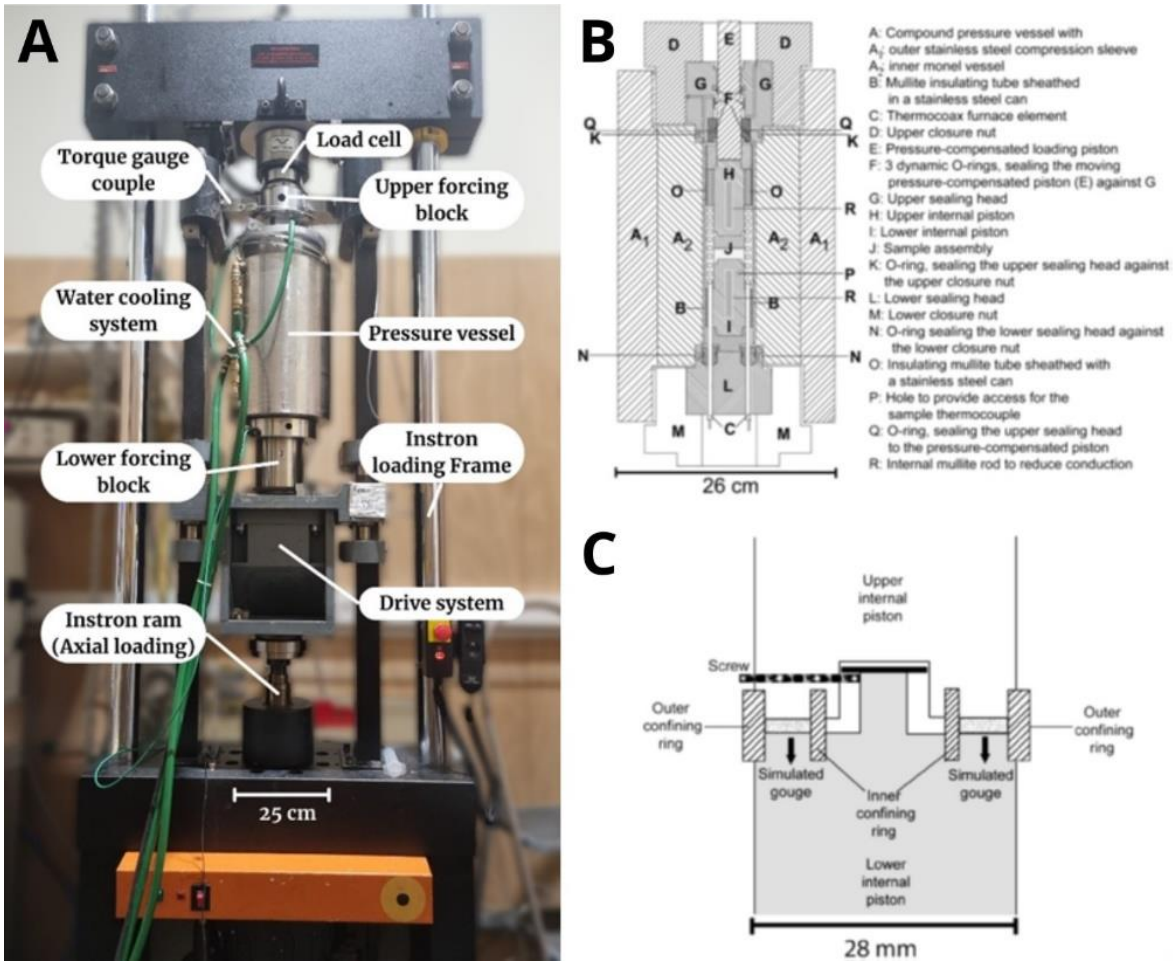

Figure 2. RS apparatus a) photograph of the RS with approximate scale. b) Schematic cross section of the pressure vessel with the internal piston inside. c) detailed cross section of the internal piston. Figure b) and c) from (Niemeijer et al., 2008).

Three different piston sets were used during the RS experiments. Sample sets 1 and 2 are made of Ni-superalloy to withstand high temperatures, while sample set 3 is made of stainless steel for experiments at lower temperatures. Between the lower and upper piston (Figure 3), material is confined between two rings with an inner and outer diameter of 22 and 28 mm respectively. These rings are coated with a molykote spray for a low friction between the sample material and the rings.

During the preparation phase, material was carefully deposited with a tiny spoon between the two rings on the lower piston and equally distributed by tapping the piston carefully on the table. Once one layer was deposited, a ring-shaped pestle was used to compact the material. This was repeated until the material was just below the top of the rings with a total weight of approximately 0.8 grams (Figure 3b). This method results in a ring-shaped gouge layer with a width of 3 mm and a thickness of approximately 1 mm. To confine the sample, the upper piston was placed on top of the lower piston and secured with a retaining screw (Figure 3). This screw prevents the two parts from disconnecting but allows for rotation without adding extra friction.

The following procedure was followed with every experiment in the RS. First, the piston was connected to the upper sealing head and placed into the pressure vessel (Figure 2b). Subsequently, the vessel was closed with the upper closure nut and loaded into the Instron loading frame. External thermocouples and the pore fluid pipe were connected. The Load was gradually increased to -1 kN (~4.24 MPa) until a plateau in friction was observed. This plateau

corresponds to the seal friction resulting from pushing through the O-ring seals, which seal the internal system (Figure 2b).

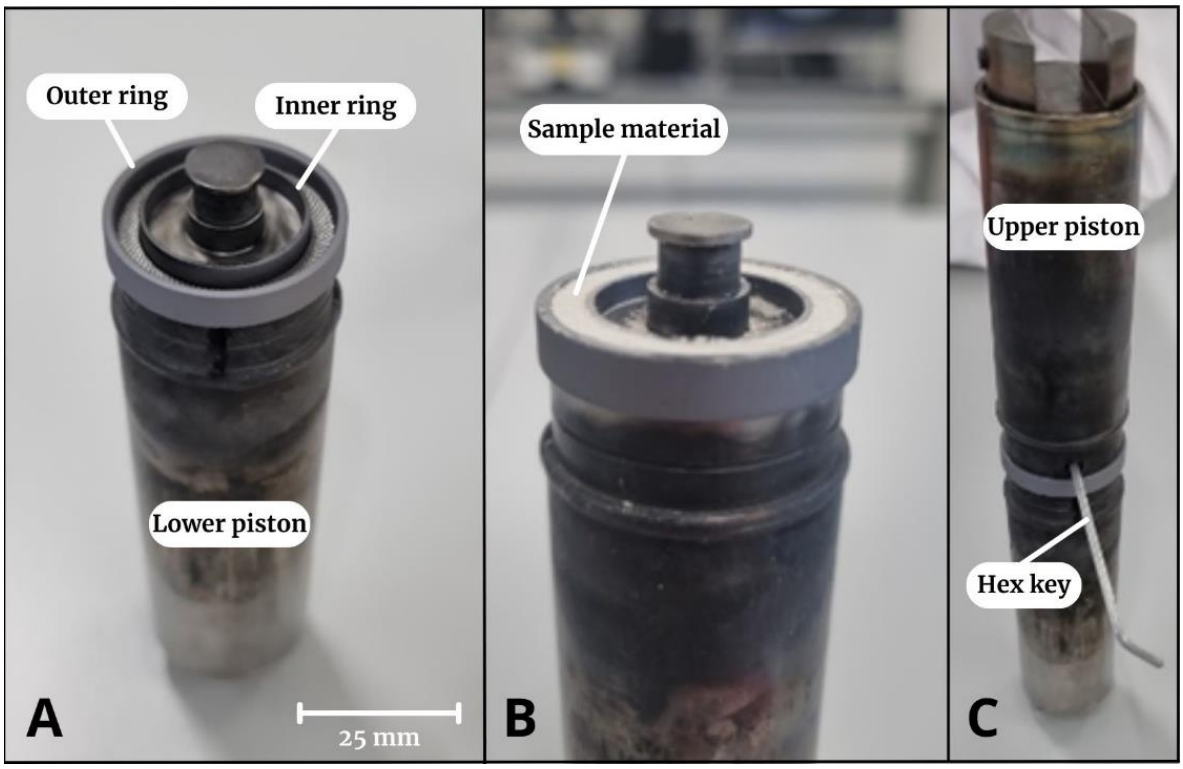

Figure 3: Photographs of RS piston assembly. a) empty lower piston with the two confining rings and a rough surface visible for friction between the sample material and piston. b) lower piston filled with smectite sample. c) lower and upper piston connected with hex key to tighten retaining screw (Figure 2c).

Next, the desired effective normal stress was applied with the Instron, using an absolute ramp setting to the target load within one minute. Upon reaching the set-point, pore fluid pressure was applied initially with an automatic piston-pump, which reached pressures of approximately 30 MPa. Additional pore fluid pressure was manually applied with a hand pump, although not fully to the experimental pore fluid pressure to prevent over pressuring due to expansion upon heating. Once the pore fluid was in equilibrium, the temperature conditions were set. When the final conditions were reached, the sample was left undisturbed for approximately 5 hours to allow the conditions inside the sample to equilibrate. After the waiting period, a short rotation was applied to increase the shear stress on the load cells. This was used to calibrate the load on both cells to a similar torque value to correct for any disbalance in the upper forcing block. A short rotation backwards was then performed to disconnect the load cells and to set the torque to zero before starting the experiment.

The SHS sequence was programmed to begin with a long sliding period (> 5000 seconds) at 1 µm/s to establish steady state sliding. During the experiments, this constant velocity sliding was periodically interrupted by reducing the driving rate to zero, initiating the hold stage. After a set amount of time, shearing was re-initiated. In most experiments, the hold times increased incrementally from 3 to 30000 seconds (steps of $\log(10^{0.5})$), with a sliding period of 600 s at 1 µm/s in between each hold.

Direct shear apparatus

In addition to experiments in the RS apparatus, direct shear (DS) experiments were conducted using a conventional triaxial deformation apparatus at the HPT laboratory of the University of Utrecht. This apparatus consists of a pressure vessel located in an Instron 1362 loading frame used for axial loading. A schematic apparatus cross section from Verberne et al. (2014) is shown in figure 4. The DS experiments were performed with a piston assembly consisting of two L-shaped parts previously described by (Verberne et al. 2013). This sample piston assembly has a specific geometry with a 1 mm thick layer of material sandwiched between the piston assembly. Each L-shaped part of the piston each has a length of 70 mm with a diameter of 35 mm. The piston consists of three different segments: a 12 mm long cylindrical end-piece, a 9 mm long smooth surface and a 49 mm long section for the sample material. The last section has groves for resistance with the gouge material and tiny holes for the pore fluid. The setup has the advantage over a classical "saw-cut" assembly because the normal stress on the sample is independent of the shear displacement, whereby the confining pressure is always the same as the normal stress.

During experiments, the axial force is transmitted from the Instron on the sample holder by a Ti-grade 5 piston with an internally located load cell to measure the axial force (Figure 4). This load cell has a full scale range of 100 kN with a resolution of 33 N. Because this load cell is internally located, it measures the axial force independent of the seal friction. Subsequently, the shear stress is calculated by dividing the axial force by the sample area. The displacement is measured by the Instron and also externally on the pressure vessel using an LVDT with a resolution of 5 µm. Additionally, the Instron load cell also measures the axial force within approximately 0.25 % on the full scale 100kN.

Around the sample piston, confining pressure is applied with an external compressed air-driven pump whereby silicone oil is used as the confining medium. The experiments were performed with demineralized water as the pore fluid pressure phase which was regulated by two additional external pumps (A and B) controlled with ISCO software withing approximately 0.05 MPa. One pump is connected to the piston through the top forcing block and the other through the lower forcing block (Figure 4b). The temperature can be applied with an internal furnace which is regulated within 0.1 °C by a temperature controller. Temperature is measured internally by a thermocouple close to the sample layer and additionally at two different locations in the confining fluid.

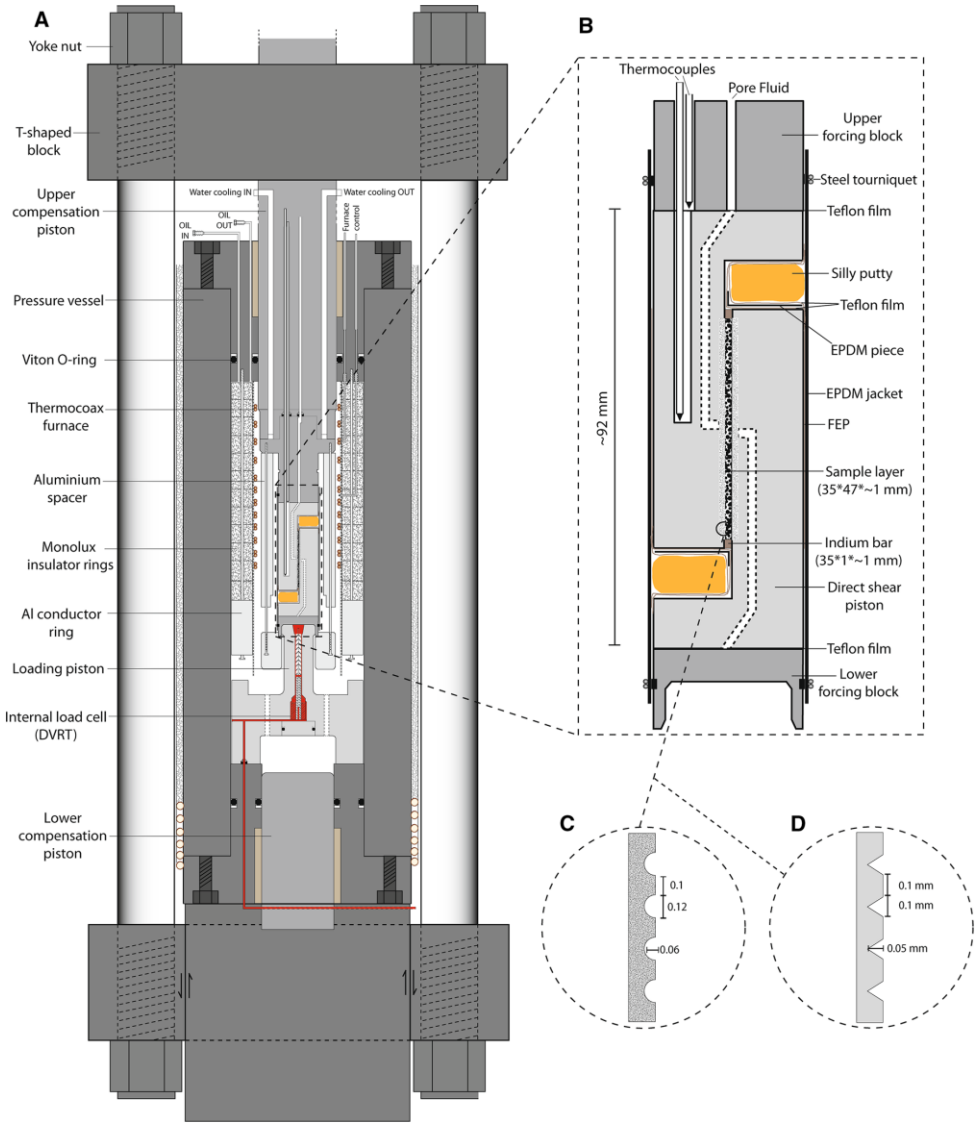

Figure 4: Schematic cross-section of the Shuttle a) apparatus with DS assembly b) detailed cross-section of the DS piston assembly. From Verberne et al. (2014). Note that in the piston assembly used for this study, also the lower forcing block has a separate pore fluid connection which is not shown in this drawing.

The samples for the DS experiments were prepared in a specific holder (Figure 5a). For OPA, 3.2 grams and for SWY-2, 4 grams of material was carefully deposited in the sample preparation holder to achieve a thickness of approximately 1 mm. The material was evenly distributed with a T-shaped flat pestle that reached 1 mm above bottom the bottom of the sample preparation holder. By gently tapping the material, an even surface was created. A metal block was placed on top of the sample and the layer was prepressed with 30 kN (~17.5 MPa) force for 120 seconds total (applied in 4 intervals of 30 seconds, with a 90° rotation between the presses) in a hydraulic press. Next, the other L-shaped piston part was placed on the opposite side of the sample with an incompressible hard spacer between the cylindrical end-pieces (on the smooth surface section) to align the piston parts (Figure 5b). A heat-shrink FEP tube was placed around the piston set to keep the pistons in place and the hard spacer was replaced by a compressible silicone polymer. This assembly was then wrapped with Teflon paper and tape. The piston was placed between two forcing blocks with connections for the pore fluid phase and a thermocouple from the upper forcing block. The two forcing blocks were connected with 3 long stabilising screws and a heat-shrink tube was shrunk around the piston to seal the assembly

(Figure 5c). A stainless steel tourniquet was used to seal the shrink tube over the O-rings located on the upper and lower forcing blocks (Figure 5d).

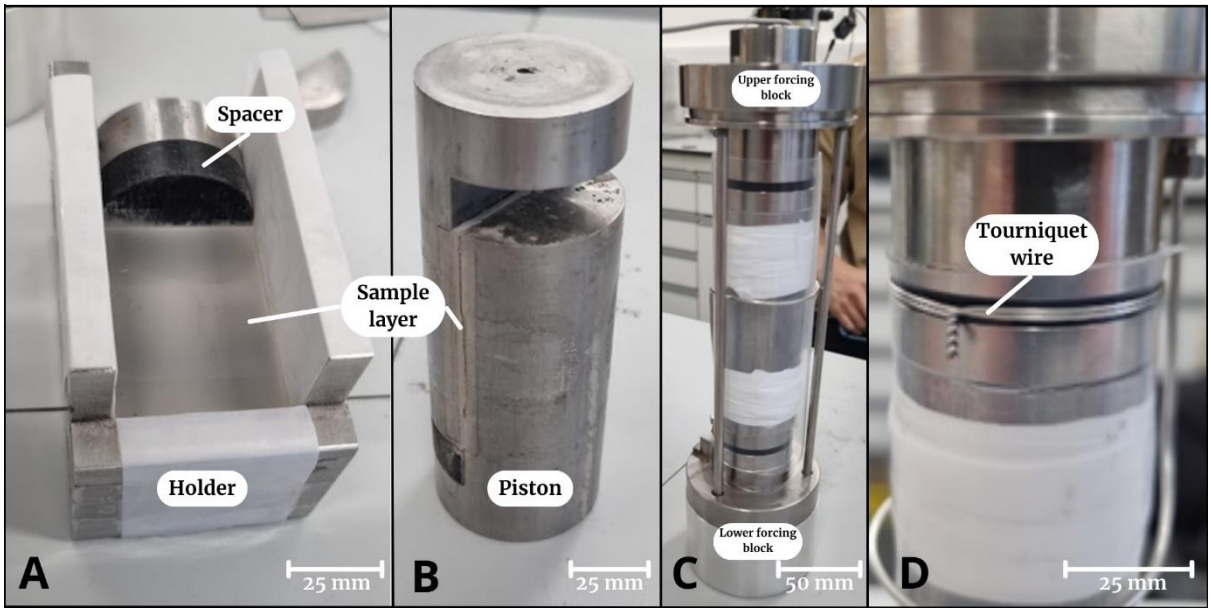

Figure 5: Photographs of a) DS holder and piston for deposition of material precisely on the rough part of the L-shaped piston. b) the two pistons with a sample layer sandwiched between the pistons. c) confined internal piston assembly connected to the lower and upper forcing blocks. d) wrapped tourniquet wire to seal the assembly.

The DS piston assembly was built into the Shuttle apparatus by connecting the assembly to the T-shaped block. Followed by lowering of the assembly into the pressure vessel and tightening of the yoke nuts (Figure 4). The experimental setup procedure began with first application of the confining pressure to achieve the desired experimental effective normal stress. Then, the pore fluid pressure was increased along with additional confining pressure in steps of 5 MPa, ensuring that the effective normal stress remained constant. The control software was set to maintain constant pressure to keep the pressure constant until the internal conditions stabilized. After stable conditions were reached, a pressure difference of 10 MPa between pump A and B was applied for a permeability measurement. For the smectite experiment, no permeability measurement was conducted due to the low pore fluid pressure. Instead, the temperature was set after establishing pressure conditions and the sample was left for over 12 hours to equilibrate.

Before preforming the SHS experiments, the seal friction was determined after the first touch. For both experiments, the sample was initially sheared at 1 µm/s until steady state friction was reached. Subsequently, holds were manually executed at specific intervals by pausing the displacement ramp on the Instron. For the Opalinus clay, holds ranged from 100 to 10000 s. During the smectite experiment, two series of 3 to 3000 s and 100 to 3000 s were performed with an increase in pore fluid pressure from 10 MPa to 20 MPa between the series.

Data processing

The recorded data from the specified measurement instruments is recorded in volts. Using calibration equations, the raw data was converted to standard units using a Python script. The calculated torque T [Nm] was converted to shear stress τ [MPa] with the average radius of the ring-shaped sample with formula 4:

$$\tau = \frac{3T}{2\pi \cdot (R_o^3 - R_i^3)} \quad (4)$$

In this formular, R_o represents the radius of the outer ring [m] and R_o the inner ring [m].

The python script was also used for further processing of the data, to correct for the seal friction and pore fluid pressure effect. Assuming that the pore fluid pressure is fully saturated in the sample, the applied normal stress is equal to the effective normal stress on the sample. To prevent the vessel from leaking, a seal is blocking the outflow of fluid (Figure 2b). This results in a small seal friction which needs to be subtracted from the applied load to obtain the effective normal stress (σ_n^{eff}). Subsequently the total normal stress is slightly changed. The friction coefficient (μ) is calculated by dividing the shear stress over the effective normal stress. The shear stress or friction coefficient data was plotted against the displacement or time. During the SHS sequences, a peak in friction is commonly observed upon resliding. After this peak, the friction decreased to a steady-state level of friction again. The difference between the peak and steady state level is defined as the frictional healing (Δμ) and the total decrease in friction (by subtracting the friction value at the end of the hold from the beginning at steady state) during the hold is defined as the creep relaxation ($\Delta\mu_c$) (Marone 1998).

The velocity dependence of friction was analysed using the Rate-and-State friction (RSF) equations (Dieterich, 1979; Ruina, 1983). In this study, the Dieterich type evolution (equation 2) was used in the RSF equation 1, as a tool to investigate the friction as a function of time. To determine the parameters a, b and d_c, a program called Xlook developed at Pennsylvania State University Mechanics Group (2014) was utilized. After measuring the stiffness, a forward method was used to make the best possible fit with the recorded data. Subsequently, an inversion technique was utilized to calculate the RSF values.

Other SHS studies have identified a general trend wherein frictional healing increasing logarithmically with hold time (Carpenter et al., 2016; Ikari et al., 2016). This trend can be expressed with the formula:

$$\Delta\mu = \beta \log_{10}(t_h) + c \tag{5}$$

In this equation, β represents the frictional strengthening rate, c is a constant and t_h the hold time. previous studies have constantly ignored c in this formula as the most important value is the frictional strengthening rate. Similar to the frictional strengthening, a trend in creep relaxation can be expressed with:

$$\Delta\mu_c = \beta_c \log_{10}(t_h) + c \tag{6}$$

Here, β_c defining the creep relaxation rate. In the results from this study, a similar logarithmical trend can be observed but only after hold times of 30 seconds. Therefore, the shorter hold times were neglected for the analysis of this these trend in this study.

The permeability k [m^2] during the DS experiment was calculated using darcy's law:

$$k = \frac{Q\mu\Delta x}{A\Delta P} \tag{7}$$

In this formula Q is the volumetric flow through the sample measured from pump A to B [m^3s^{-1}], μ the dynamic viscosity [Pa s], Δx the thickness of the sample [m], A is the area of the sample [m^2] and ΔP the pressure difference between the pumps [p.a]

Experimental conditions

Various experiments were conducted under differing conditions in order to study the effect of temperature, effective normal stress and pore fluid pressure on the time-dependent healing mechanisms. During each experiment, two SHS series were executed with different pore fluid pressures by changing the pressure after the first SHS sequence. Experiments on the Opalinus clays were performed with different temperature and pore fluid pressure conditions. For experiments on smectite, the effective normal stress was also varied across for different experiments. All the other conditions were held constant when varying those conditions. Table 1 shows the conditions for each experiment, additional material and SHS procedure data is stored in Appendix A. During all experiments the driving rate during sliding was 1 µm/s.

Table 1: Experimental conditions for the experiments. RS experiments are indicated with "u" and direct shear with "ds".

Experiment	Material	Temperature (°C)	Effective normal stress	Pore fluid pressure
u1196	OPA 1	80	50 MPa	Vacuum
u1198	OPA 1	80	50 MPa	50 - 1.5 MPa
u1200	OPA 2	80	50 MPa	50 - 1.5 MPa
u1202	OPA 3	80	50 MPa	50 - 1.5 MPa
u1203	OPA 3	120	50 MPa	50 - 1.5 MPa
u1205	SWy-2	80	50 MPa	50 - 1.5 MPa
u1206	OPA 3	20	50 MPa	50 - 1.5 MPa
u1210	SWy-2	120	50 MPa	50 - 100 MPa
u1211	SWy-2	120	50 MPa	10 - 1 MPa
u1212	SWy-2	120	25 MPa	50 -10 MPa
u1217	SWy-2	120	75 MPa	50 - 10 MPa
u1218	SWy-2	80	25 MPa	50 - 10 MPa
u1221	SWy-2	20	25 MPa	50 - 10 MPa
u1222	SWy-2	80	25 MPa	50 - 10 MPa
u1223	SWy-2	120	37.5 MPa	50 - 10 MPa
u1224	SWy-2	120	62.5 MPa	50 - 10 MPa
dsOPA	OPA 3	20	25 MPa	25 MPa
dsSWy	SWy-2	120	25 MPa	10 - 20 MPa

Results

Materials

The results from the TGA analysis (Table 2, Appendix B) show that the three Opalinus batches differ in composition. Smectite has a characteristic thermogravimetric curve with dehydration peaks that correlate to the intervals at 1 and 4 (20-300 °C and 600-800 °C) (Földvári, 2011). This suggests that OPA 2 has the lowest smectite content because no peaks and thus weight loss was observed at 600-800 °C. Both OPA 1 and 3 both have higher smectite concentration because more dehydration took place during interval 1 and 4. The varying sizes of the dehydration peaks suggest that the overall composition of the OPA batches differs. Additionally, the dehydration of calcite and other minerals occurs at 600-800 °C as well (Földvári, 2011), which indicates that the SWy-2 sample could also contain other minerals besides smectite (Chipera & Bish, 2001). A second SWy-2 measurement (SWy-2b) was performed on the smectite material after experiment u1221 in order to investigate is the composition changes after material loss in the RS. SWy-2b show only minimal decrease in dehydration intervals 1 and 4 compared to the SWy-2 before the experiments.

Table 2: Results from the TGA measurements. The table shows the weight loss percentage at specific temperature intervals where peaks were observed for the different materials.

Material	Sample Weight	Interval 1 T: 20-300°C	Interval 2 T: 300-500°C	Interval 3 T: 500-600 °C	Interval 4 T: 600-800 °C	Residue T: >800 °C
OPA 1	28.504 mg	2.51 %	4.16 %	2.27 %	8.09 %	82.87 %
OPA 2	21.442 mg	3.12 %	3.36 %	4.32 %	-	88.70 %
OPA 3	21.588 mg	3.51 %	4.25 %	1.67 %	6.49 %	84.08 %
SWy-2	27.844 mg	11.16 %	-	-	4.45 %	84.39 %
SWy-2b (u1221)	30.571 mg	10.37 %	-	-	4.25 %	85.37 %

Additionally, the particle size distribution of smectite was measured before and after the experiments (Figure 6). A mixture of u1222 and u1223 was utilized for the analysis from the RS and dsSWy material was used from the DS. The results indicate a higher fraction of the larger particles (200-500 µm) in the original smectite sample. However, post-experiment analysis reveals a reduction in this fraction because the curve shows a smaller volume percentage of big particles after the experiments.

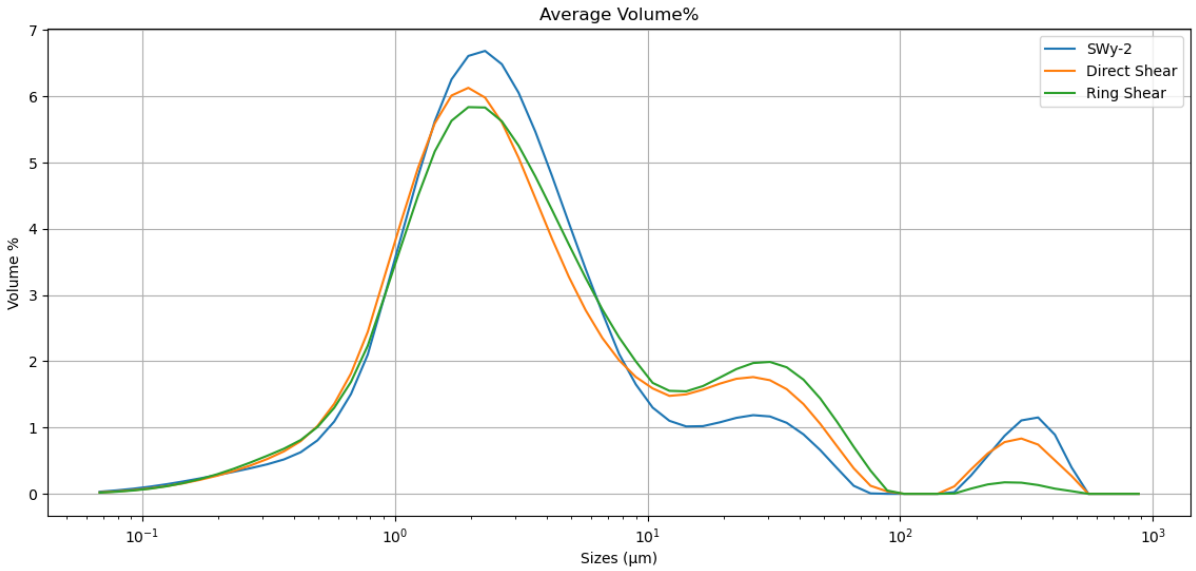

Figure 6: Particle size analysis for SWy-2 before and after the DS and RS experiments. Volume percentage is plotted against the particle size intervals.

Shear stress evolution with displacement

During the RS experiments, the shear stress continuously evolves with displacement and time. Figure 7 shows the evolution of the shear stress for experiments performed on OPA and SWy2. For every experiment, two SHS series can be observed which can be distinguished by a big drop in shear stress between the series. This drop is attributed to the change in pore fluid pressure between the two series and the additional wait time before the new conditions have equilibrated. Some experiments have different SHS sequences due to the adjustments made in the protocol to obtain the best frictional healing results.

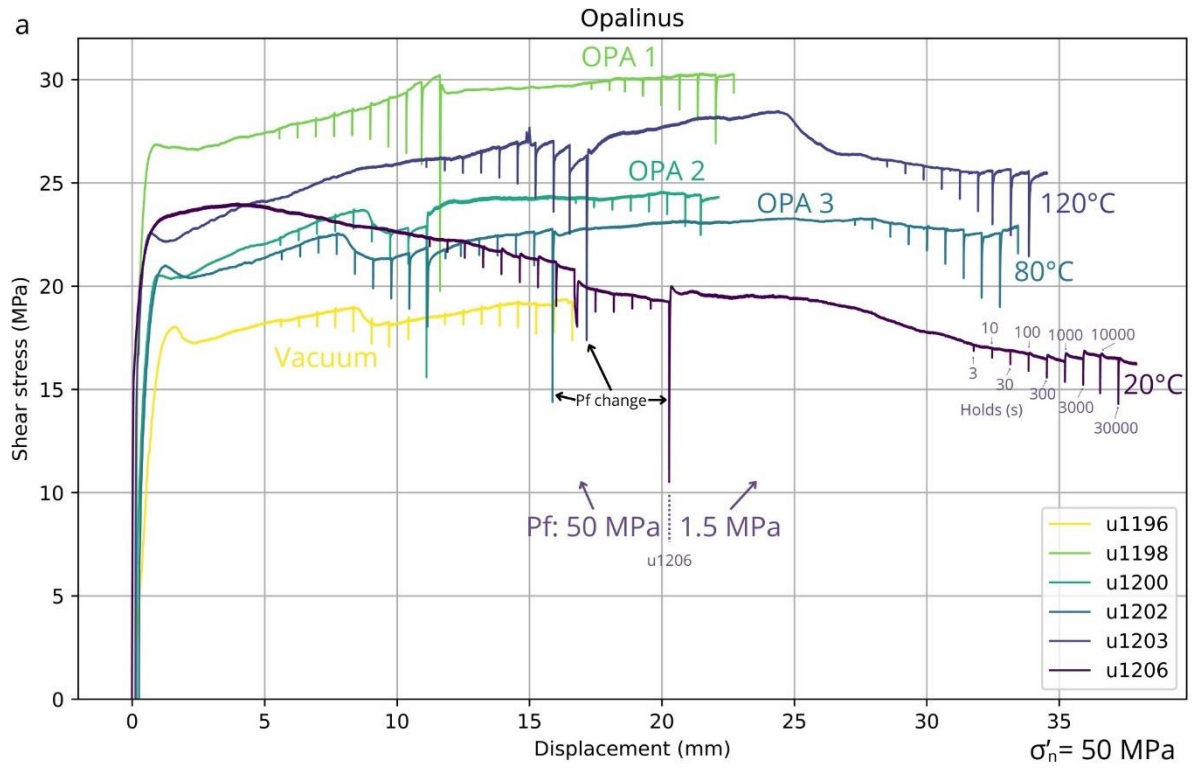

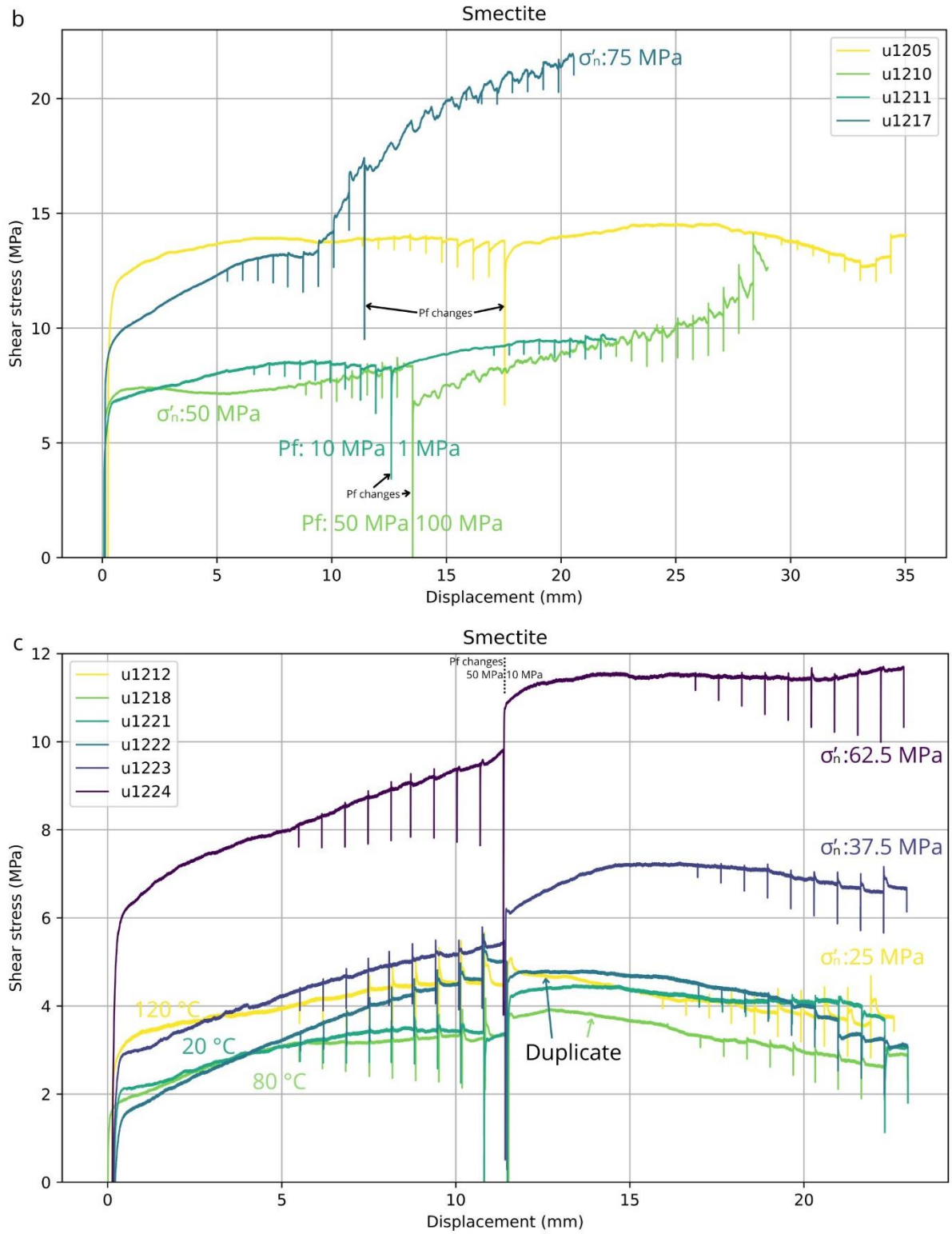

Figure 7: Shear stress evolution as a function of the total load-point displacement of the RS experiments on a) Opalinus and b/c) Smectite. Conditions as indicated in the plot.

Details of a single SHS test

Figure 8 shows a detailed plot of a single SHS test with a hold of 1000 seconds. The friction coefficient is shown as a function of both the displacement (blue) and time (red) on different x-axes. Labels indicate the hold and reload start points. The friction coefficient decreases when the hold begins until the reload point. Upon reloading, the friction coefficient increases until the peak static friction value is reached followed by a decrease to the steady state sliding. The definitions for the steady state friction ($\Delta\mu_{ss}$), frictional healing ($\Delta\mu$) and creep relaxation ($\Delta\mu_c$) have been indicated with labels.

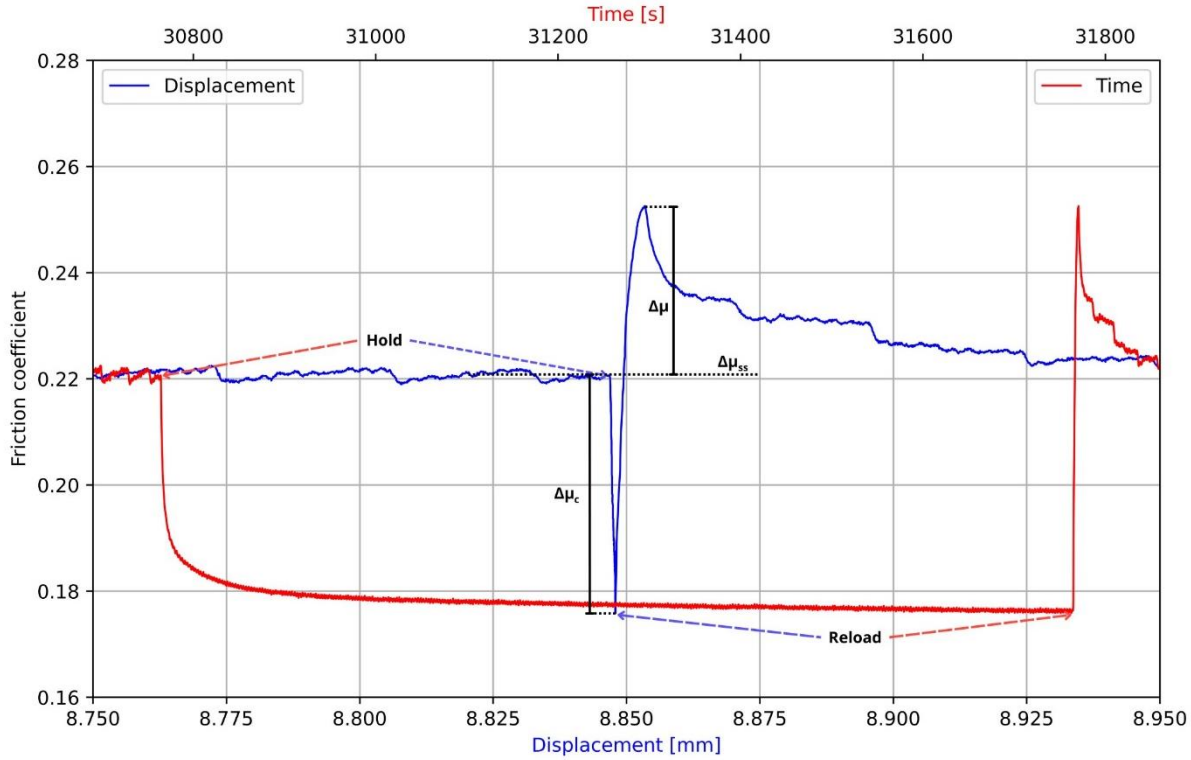

Figure 8: Friction coefficient in a single SHS test from experiment u1212. Note that there are two x-axis scales with blue showing the friction coefficient evolution over displacement (mm) and the red curve over time (s).

The two different series of every experiment will be labelled, with the first series receiving the letter "a" behind the experiment number and the second series label "b". For example, the first series of experiment u1212 which was done under 50 MPa pore fluid pressure will be denoted as u1212a, while the second series at pf = 10 MPa will be referred to as u1212b.

Frictional healing and creep relaxation

Frictional healing and creep relaxation were measured for different hold periods in all experiments. The results from experiments on OPA demonstrate no systematic changes in the amount of healing or creep relaxation with temperature or pore fluid pressure. The maximum frictional healing that was measured for Opalinus was below $\Delta\mu$ = 0.005 with the majority (<95%) of the data below $\Delta\mu$ = 0.003. In contrast, results from experiments on SWy-2 exhibit more systematic changes in the amount of healing with varying conditions, as shown in figure 9. Overall, the frictional healing increases with time. Plotted on a normal scale the data has an increasing concave down fit that roughly follows the function y=a ln(x) – b. Because the hold times increase with steps of $\log(10^{0.5})$, the x-axis will be shown in a logarithmic scale for easier visualization.

Experiments with similar conditions and with only one variable parameter were plotted on the same figure. The effect of temperature, effective normal stress and pore fluid pressure are shown (Figure 9) and the following trends can be observed:

Experiments with different temperature conditions of 20, 80 and 120 °C were performed with an effective normal stress of 25 MPa and pore fluid pressures of 50 MPa. Figure 9a shows the effect of temperature on the frictional healing (Δμ) during the different hold periods. The results demonstrate a positive correlation between temperature and frictional healing, with higher temperatures leading to increased healing.

Five different experiments with varying effective normal stress of 25, 37.5, 50, 62.5 and 75 MPa have been performed at 120 °C and with a pore fluid pressure of 50 MPa (Figure 9c). These experiments indicate that a lower effective normal stress results in more frictional healing.

The effect of pore fluid pressure on the frictional healing has been studied with experiments with 1, 10, 50 and 100 MPa pore fluid pressure with a temperature of 120 °C and an effective normal stress of 50 MPa (Figure 9e). These results demonstrate that higher pore fluid pressures lead to increased frictional healing.

The creep relaxation results are depicted in figure 9b/d/f. Overall, the amount of creep relaxation increases with longer hold times. When plotted on a logarithmic scale, the curve initially shows an increasing concave-down shape followed by a roughly linear pattern, although some experiments deviate from that fit. Temperature exhibits minimal to no effect on creep relaxation. At 120 °C, higher creep relaxation is observed for short holds ($t_{hold} < 100$ s), while lower creep relaxation is observed for longer holds ($t_{hold} > 10000$ s) but the difference is less than $\mu_c = 0.01$.

The effective normal stress and pore fluid pressure both have an effect on the creep relaxation with lower effective normal stress and higher pore fluid pressures resulting in more creep relaxation. In some experiments, the creep relaxation saturates at longer hold times whereas others start to exponentially increase at a certain point. This can be observed in for example experiment u1211b (Figure 9f), where after the 300 s hold, the creep relaxation increases significantly compared to the other trends. This increase appears to have a negative effect on the frictional healing which decreases at the same time the creep relaxation increases.

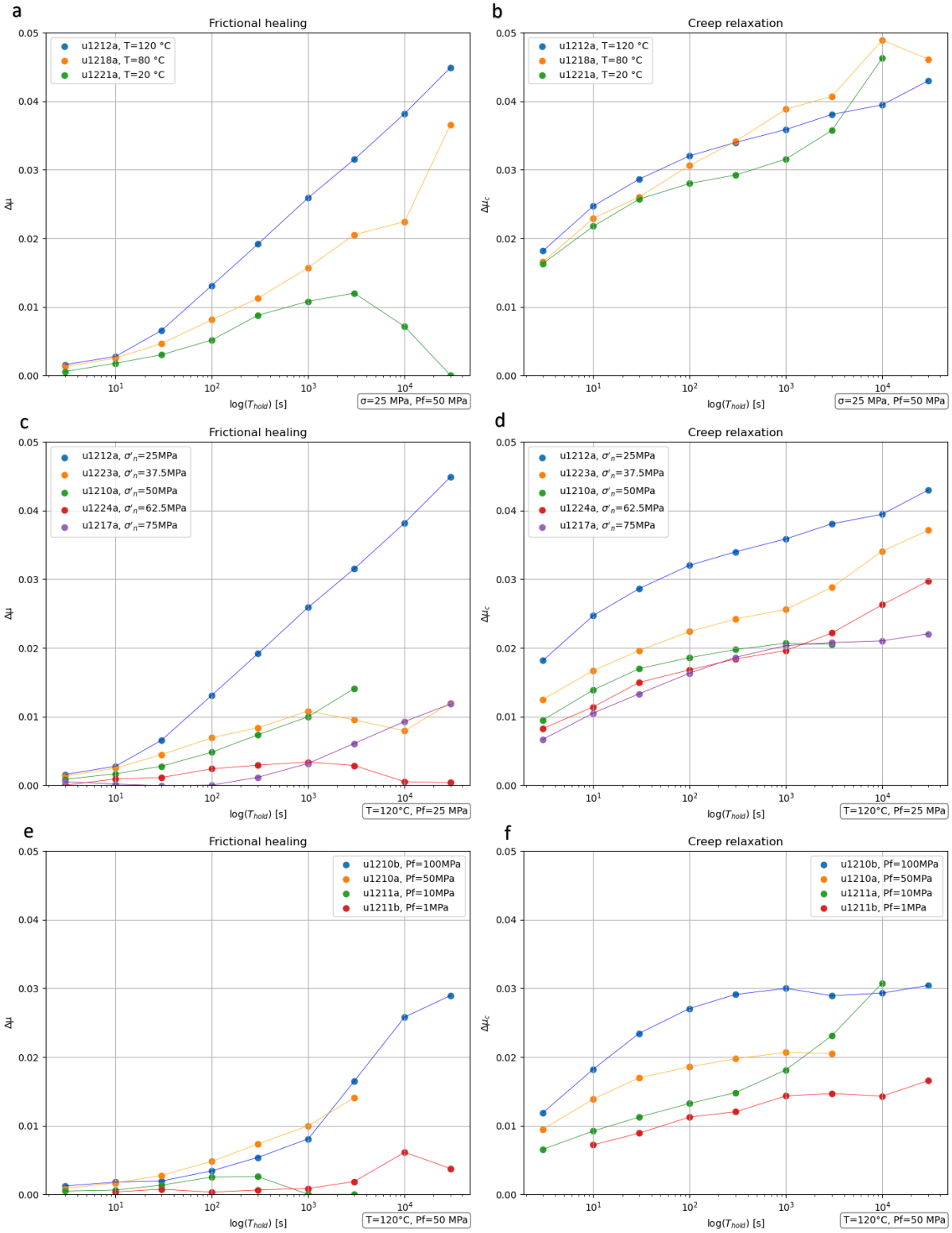

Figure 9: Frictional healing (a/c/e) and creep relaxation (b/d/f) values plotted against the hold times on a logarithmic scale divided in experiments with similar conditions and with variable temperature (a/b) effective normal stress (c/d) and pore fluid pressure (e/f).

Frictional strengthening and creep relaxation rates

With the overall trends of the friction coefficient and creep relaxation, loglinear fits were obtained to calculate the frictional strengthening rates (β) (equation 5), and creep relaxation rates (β_c) (equation 6), displayed in Table 3. The coefficient of determination (R^2) is given along with the number of data points (n) used for the trendline. The amount of data points is lower for some experiments when the data deviates from the log linear trend as can be seen in figure 9 (e.g. exp u1211a in figure 9f/g). The same temperature, effective normal stress and pore fluid pressure effects on the frictional strengthening rates can be observed as described above for the frictional healing plots.

Table 3: Frictional strengthening and creep relaxation rates for different experiments. 'n' values indicate the of amount of datapoints used for the trendlines.

Experiment	μ_{ss}	β (x10^{-3}) [log(s^{-1})]	R^2	n	β_c (x10^{-3}) [log(s^{-1})]	R^2	n
u1205a	0.275 - 0.280	1.64	1.0000	2	4.28	0.9725	6
u1205b	0.266 – 0.282	0.73	1.0000	2	2.33	0.9973	5
u1210a	0.151 – 0.162	5.56	0.9793	5	4.28	0.9118	6
u1210b	0.187 – 0.238	6.72	0.8557	5	7.21	0.9230	6
u1211a	0.166 – 0.170	1.26	0.8075	3	4.37	0.9920	6
u1211b	0.183 – 0.190	3.40	0.7664	4	3.47	0.9804	5
u1212a	0.162 – 0.182	12.53	0.9999	6	6.82	0.9444	6
u1212b	0.143 – 0.169	11.44	0.9555	5	4.59	0.9618	6
u1217a	0.167 – 0.212	3.81	0.9115	6	5.44	0.9852	6
u1217b	0.270 – 0.284	1.76	0.8539	5	3.36	0.9982	6
u1218a	0.126 – 0.134	7.43	0.9898	6	8.53	0.9938	6
u1218b	0.114 – 0.133	2.74	0.9895	5	6.05	0.9856	6
u1221a	0.126 – 0.139	4.73	0.9725	5	5.75	0.9383	6
u1221b	0.147 – 0.167	4.80	0.9999	3	5.80	0.9930	6
u1222a	0.136 – 0.184	6.30	0.9958	5	8.18	0.9802	6
u1222b	0.129 – 0.180	5.40	0.7550	3	9.80	0.9890	6
u1223a	0.116 – 0.143	3.78	0.9906	5	5.17	0.9668	6
u1223b	0.176 – 0.192	2.88	0.9939	5	5.95	0.9807	6
u1224a	0.130 – 0.152	1.45	0.9386	4	4.53	0.9576	6
u1224b	0.182 – 0.186	2.87	0.8936	3	4.70	0.9970	6

Rate-and-State friction

The temperature, effective normal stress and pore fluid pressure dependency of the Dieterich Rate-and-State friction parameters (Dieterich 1979) are shown in figure 10. Most experiments demonstrate a downward *a-b* trend with the lowest values at longer holds. For lower temperatures, this trend is not clear but for 120 °C a steeper downward trend can be observed. The effective normal stress has little effect on the *a-b* value with all measurements showing a similar trend for the range in conditions. For the experiment with an effective normal stress of 75 MPa, no RSF inversion was possible because of the absence of clear peaks in shear stress. The pore fluid pressure seems to have an effect on the *a-b*, with a steeper downward trend for higher pore fluid pressures. The *a* and *b* are shown separately in figure 11 and give information about the direct and evolutionary effects.

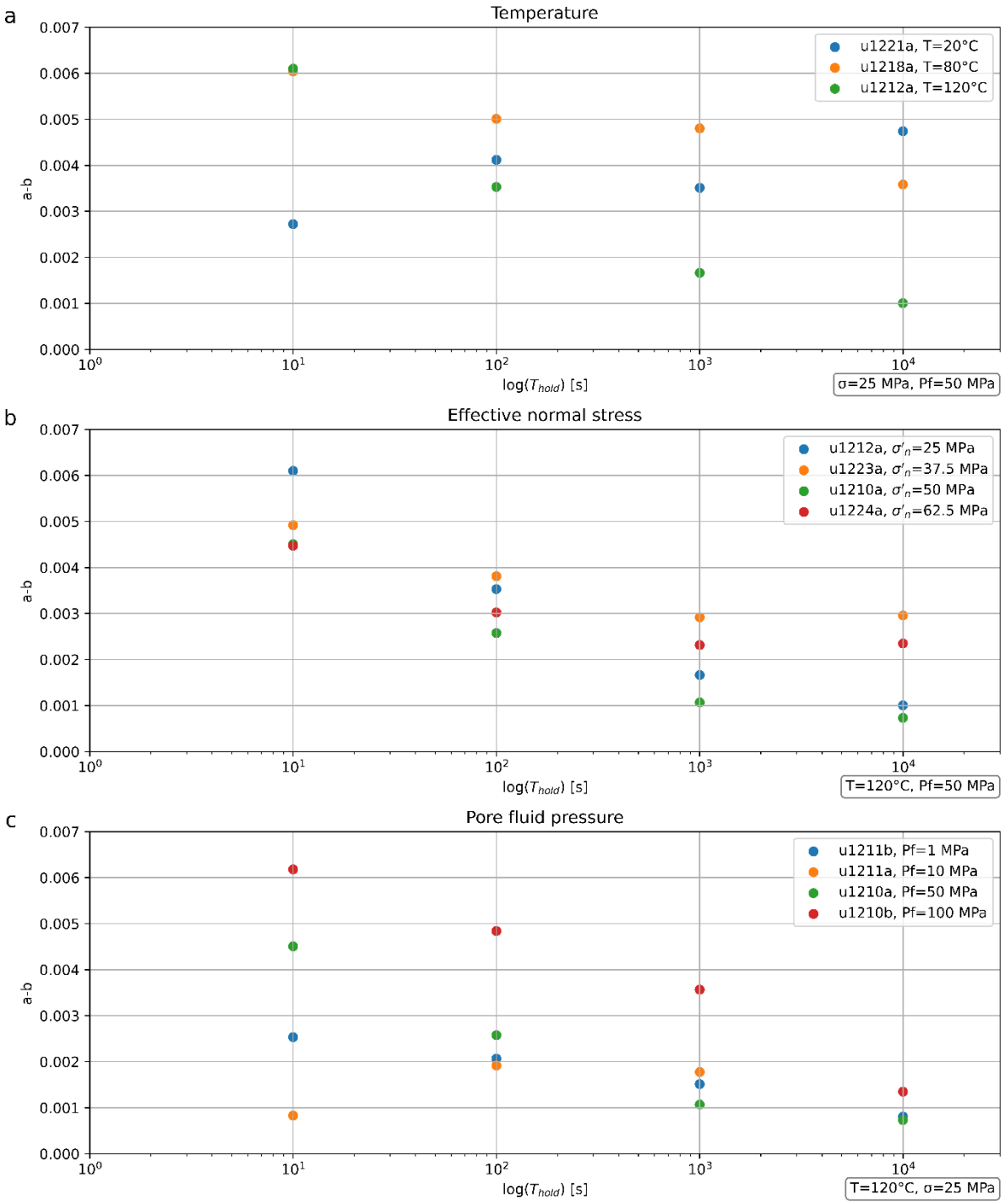

Figure 10: RS friction values of a-b as a function of the hold time. Effect of a) temperature, b) effective normal stress and c) pore fluid pressure has been shown in separate plots.

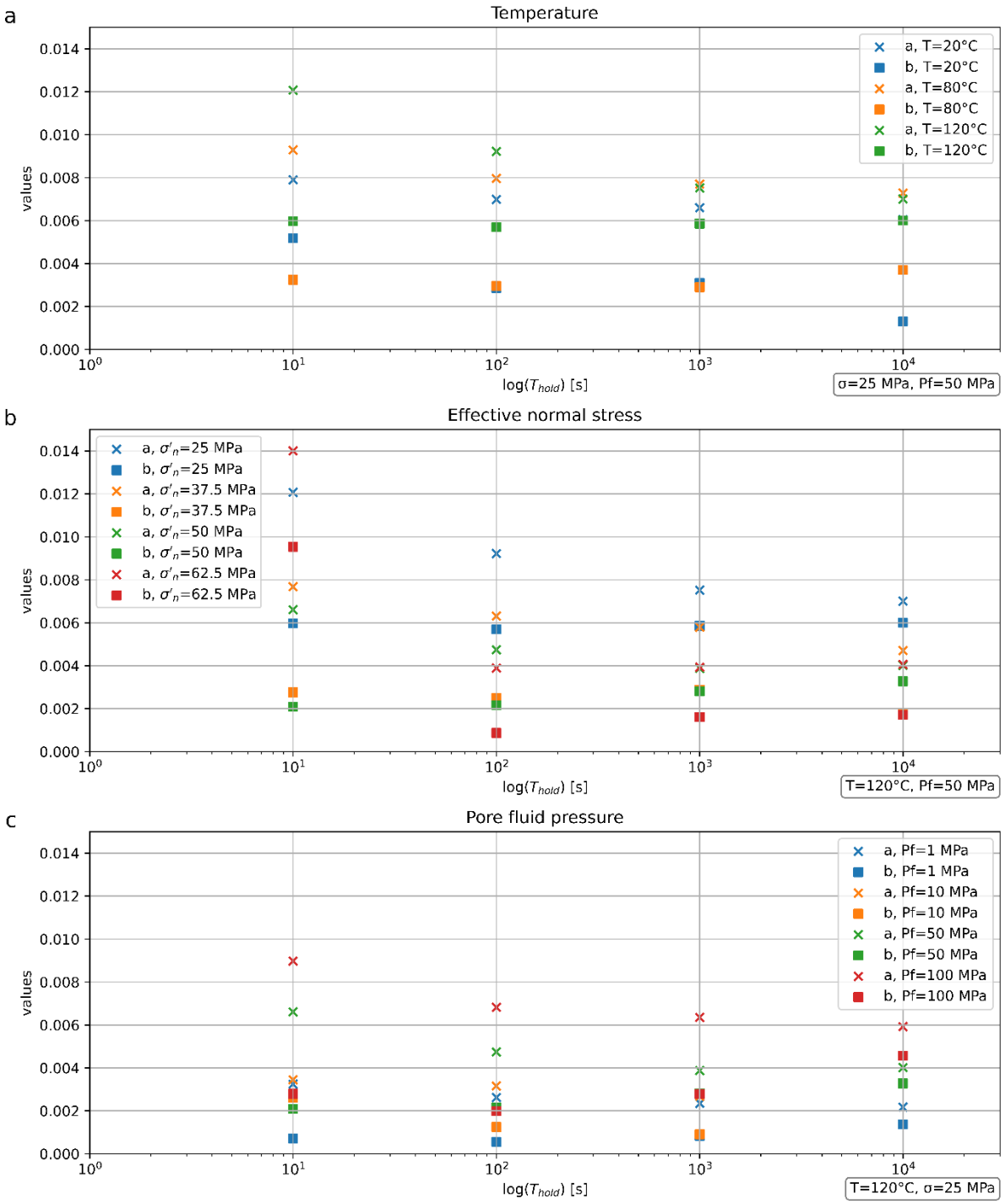

Figure 11 RS friction values a (crosses) and b (squares) as a function of the hold time. Effect of a) temperature, b) effective normal stress and c) pore fluid pressure has been shown in separate plots.

Direct shear experiment

The evolution of the coefficient of friction as a function of the total displacement of the DS experiments have been shown in figure 12. The coefficient of friction was measured from the axial force from two locations, internally and externally in line with the Instron load frame which are both plotted separately. The recorded Instron data is slightly lower and is more irregular. There are no prominent peaks visible as were observed in the RS data. However, there seems to be an increased friction visible especially in the Instron data after resliding for longer holds.

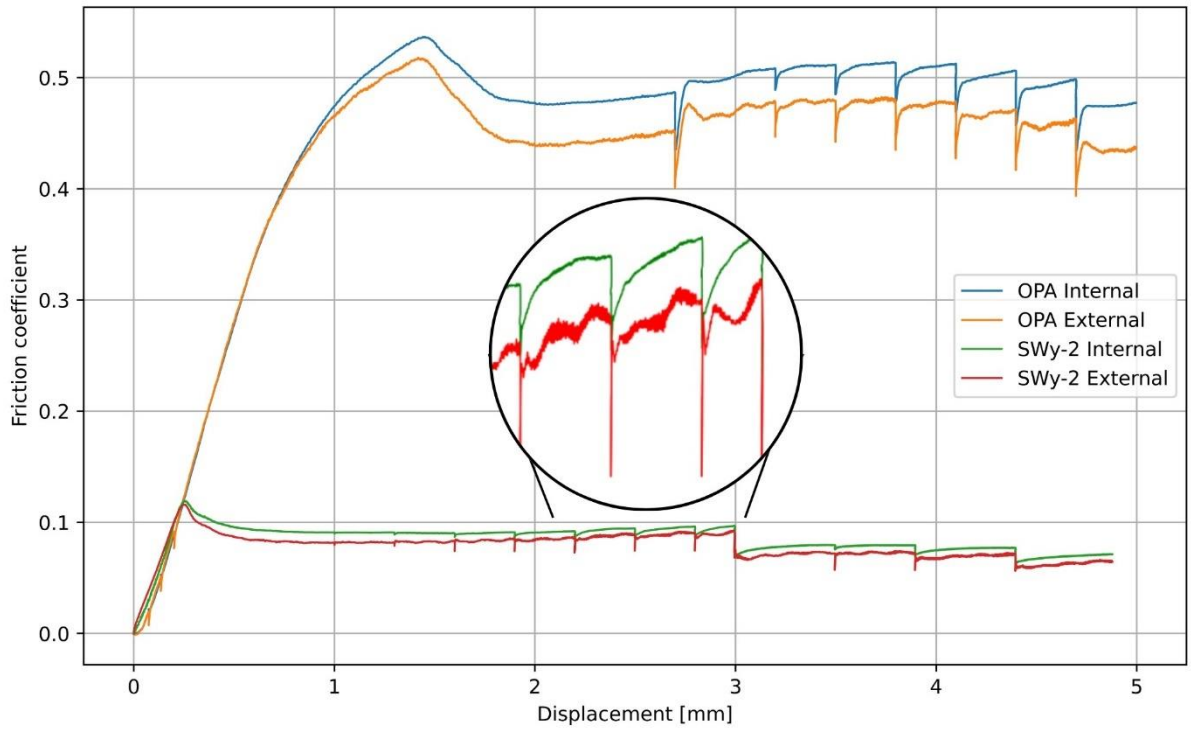

Figure 12: DS evolution of the coefficient of friction as a function of the total displacement. The internal in external recorded data is plotted separately. The last section of the first series of the SWy-2 experiment is magnified in the circle.

The creep relaxation of the DS has been measured and compared to RS experiments with similar conditions (Figure 13). RS experiment u1206 on OPA shares the same temperature conditions as the DS experiment on OPA and exhibits a similar relaxation behaviour. The RS smectite experiment u1212b was performed under the same conditions as the DS smectite experiment, except for the second SHS sequence in the DS which has a higher pore fluid pressure of 20 MPa. The comparison demonstrates that the creep relaxation of smectite in the DS is significantly lower than in the RS. The coefficient of friction values are also similar for the OPA experiments and differs for smectite between the RS and DS. Values for OPA are between $\Delta\mu_{ss}$ = 0.41-0.45 in the RS and $\Delta\mu_{ss}$ = 0.45-0.52 in the DS. For smectite valus of $\Delta\mu_{ss}$ = 0.14-0.17 in the RS and $\Delta\mu_{ss}$ =0.09-0.1 in the DS were measured.

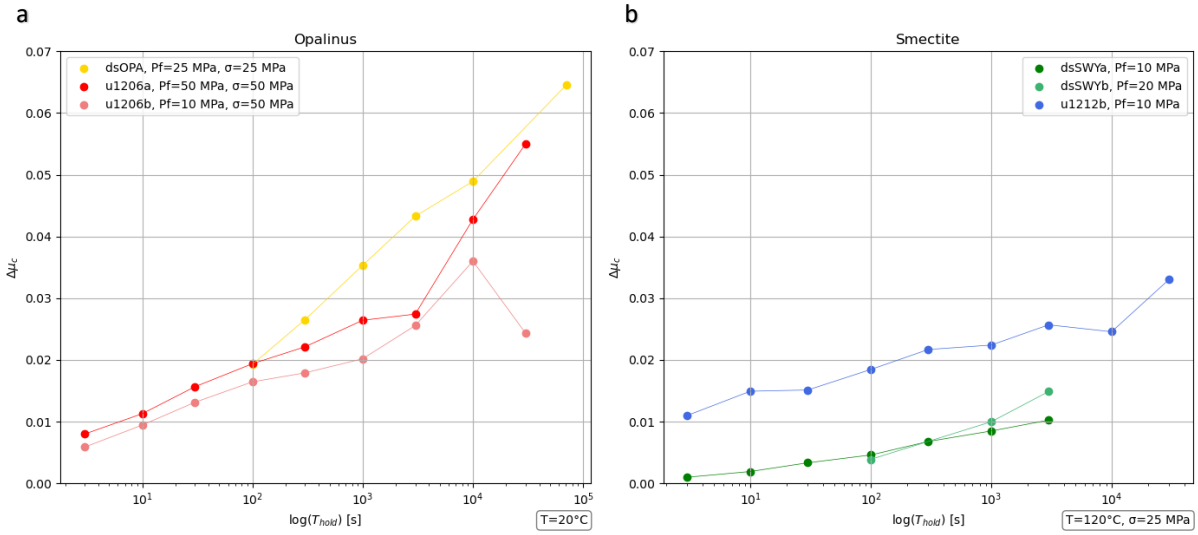

Figure 13: Creep relaxation comparison of DS and RS experiments for a) Opalinus clay and b) smectite.

Permeability

The permeability of Opalinus clay was measured during the DS experiment. Figure 14 shows the permeability during the first part of the SHS sequence. Upon sliding, a small increase in permeability (<5 x 10^{-20} m^2) was observed, followed by a gradual decrease in permeability during the hold.

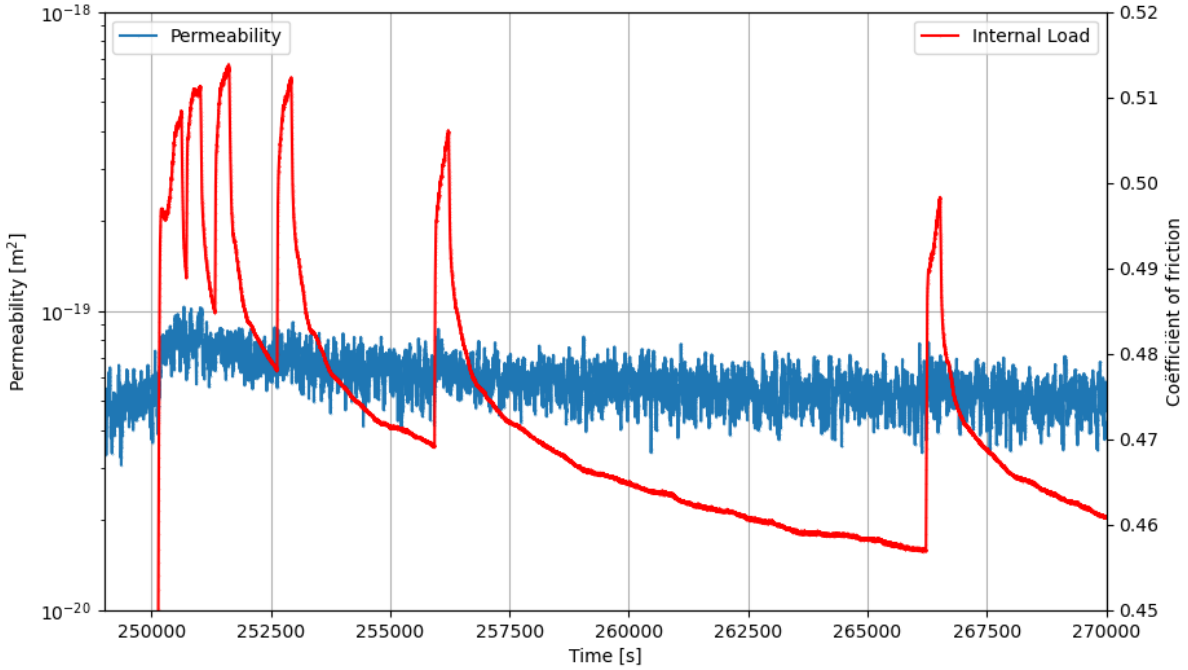

Figure 14: Permeability measurement during the first part of the SHS sequence of the Opalinus clay DS experiment.

Minimum reproducibility error

The reproducibility of experiments was assessed thought two identical experiments (u1218 and u122) to quantify the minimum error. Figure 15 displays the frictional healing and creep relaxation of the duplicate experiments, with labels indicating the minimum error in Δμ for each hold. The first SHS series of both experiments (at 50 MPa pore fluid pressure) demonstrate similar results with only minor differences in frictional healing, especially for the shorter holds. However, for the second sequence at 10 MPa pore fluid pressure, the results were significantly different with u1222b showing significantly less frictional healing. When comparing the creep relaxation, experiment u1222b has an increased creep relaxation compared to u1218b.

Two key points can be noticed from the duplicate experiments in the RS. Firstly, the minimum error in frictional healing increases with longer hold times. Secondly, the second SHS sequence, with more displacement and a lower pore fluid pressure, also has a larger minimum error.

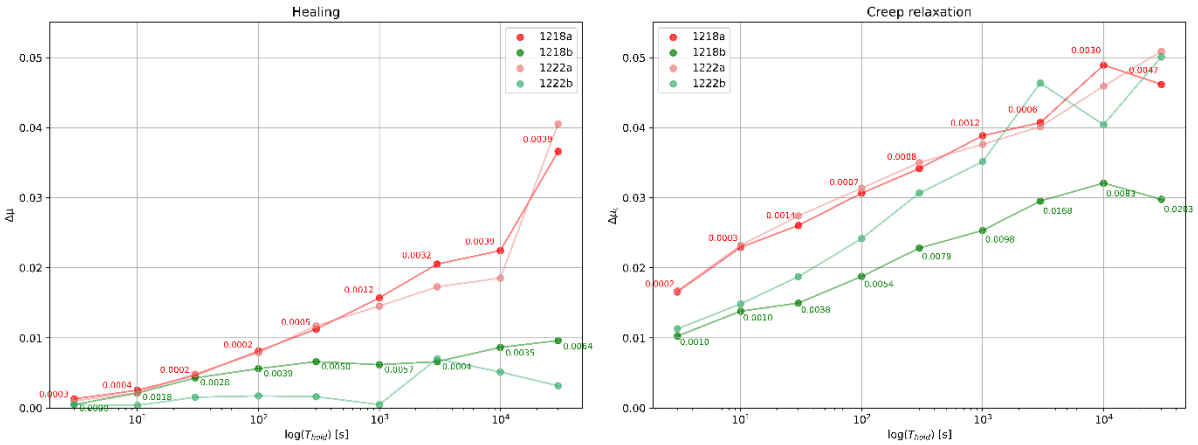

Figure 15: Frictional healing (a) and creep relaxation (b) as a function of hold time for two identical experiments u1218 and u1222. Labels indicate minimum absolute error, which is the deviation from the two measurements.

Discussion

In this study, I investigated the time-dependent healing mechanisms of smectite-rich fault gouge by performing SHS friction experiments in the hydrothermal RS apparatus with varying experimental conditions. The hydrothermal RS is the most suitable apparatus for this study because of the advantage of theoretically infinite displacement possible. Additionally, this machine is able to simulate elevated hydrothermal conditions which is not done in most other studies performed on smectite or mixtures of smectite-rich clay gouges (Kubo and Katayama 2015; Morrow et al. 2017). Understanding the healing mechanisms that control frictional healing is crucial for developing models to predict subsurface stability and how fault healing responds to changing conditions from practices such as geothermal energy and gas exploration. This study contributes to the identification and understanding of the time-dependent healing mechanisms operating in smectite-rich fault gouge. This is accomplished through an in-depth analysis of changes in the amount and rate of frictional healing under various boundary conditions in the hydrothermal RS apparatus. The type of healing mechanism and RSF information can be applied in geomechanical models to assess the stability of the subsurface to provide seismic risk advice in areas where smectite-rich clays are found.

Material properties

Experiments were performed on different batches of Opalinus clays and smectite. Results from the TGA analysis indicate that the compositions of the Opalinus clay batches differ significantly and that the smectite content is less than 33 wt% on the basis of a comparison with the measurement on SWy-2 (Table 2). A unknown during the TGA analysis is the humidity of the material used for the analysis. Because the TGA analysis of the material after the RS and DS experiments was conducted in March instead of October for the other measurements, the humidity might vary between these months which influences the relative weight percentage of the intervals. The weight change at 600-800 °C indicates that SWy-2 also contains other materials. Previous XRD studies on SWy-2 found that the material consists of approximately 75% of smectite, 18% feldspar, 8% quartz and traces of gypsum, mica and/or illite (Chipera & Bish, 2001). These authors investigated particles smaller than 2 microns and concluded that the fraction <2 µm consists of 95% smectite which indicates that the feldspar and quartz minerals have larger grain sizes (Figure 6). Generally smectite minerals are not larger than 2 microns but the bigger fractions also can consist of smectite because of cement keeping the smectite minerals clumped together (Emmerich, 2013).

The TGA results indicate that during the friction experiments, the fraction of grains between 200-500 µm decreases by about 25% in the DS and more than 80 % during the RS experiments (Figure 6). The difference between the apparatuses is probably the result of the larger total displacement in the RS (23.5 mm) compared to the DS (4.8 mm) because the conditions of the two experiments were otherwise similar. However, during the RS experiment, material is always lost which can affect the grain size distribution. It is possible that smaller particles more easily escape the confining rings, leaving the bigger particles behind. This would mean that even more reduction of bigger particles took place than what was observed and can also explain why there is a significantly bigger volume percentage of particles between 10 and 100 µm found after the RS experiments. This volume fraction is not possible to originate from the crushing of larger particles during the experiments. Instead, the loss of smaller particles results in an apparent increase in relative volume percentage of the remaining bigger particles.

Smectite has an extremely low permeability making it difficult to measure. Chu and Wang (2023) investigated the pore fluid pressure of smectite during frictional sliding and found that a lower permeability results in large variations in pore fluid pressures during sliding. These local difference in pore fluid pressure consequently influence the frictional behaviour of the material. The permeability of smectite was measured by Ikari et al. (2009) before and after shearing These authors found that the permeability decreased as the result of shearing from 1.1×10^{-17} to 2.6×10^{-16} m^2 before to values between 1.7×10^{-20} and 2.5×10^{-19} m^2 after shearing. The permeability values after shearing reported by Ikari et al. (2009) are consistent with values from this study (Figure 14). However, in contrast to Ikari et al. (2009), I observed an opposite effect with a slightly increases in permeability during sliding (<5 x 10^{-20} m^2) and decreases during the holds (2 x 10^{-20} m^2 for T_{hold} = 300 s). Different factors can influence the permeability during the experiment. Firstly, dilatancy or consolidation affects the porosity of the material, leading to varying permeabilities. Additionally, the rearrangement of the particles during sliding can affect the permeability. For increase, an increase in permeability might be measured when grains rearrange in a way that fluid is able to pass more easily through the sample.

In this study, the permeability calculation is based on the change in volume of the pumps. This means that if the material compacts, water is consequently pushed out towards the pump with the lowest pressure, resulting in a higher calculated permeability because of the compaction. Furthermore, the thickness of the sample also gradually decreases due to shearing in the DS setup. Compaction was not measured and the thickness was assumed to be constant while calculating the permeability (equation 7). If the Δx value used for the calculation is greater than the actual thickness, it results in an incorrect higher permeability. However, because the changes in permeability are very small, future experiments with special apparatus needs to be developed that can measure the permeability more precisely and will help in understanding of the changes during sliding.

It is also important to have a fully drained system with uniform fluid pressure throughout the sample when comparing results of the experiments. The time needed for pore fluid pressure to reequilibrate after disturbance can be estimated with the following formula from Ikari et al. (2009):

$$t = \frac{h^2 \beta_p \eta}{2k} \tag{8}$$

In this formula, the *h* represents the thickness of the layer [m], β_p the compressibility of the porous matrix which is approximately 2.1 x 10^{-6} m^2/N to 6.9 x 10^{-6} m^2/N for smectite (Domenico & Mifflin, 1965). η is the dynamic viscosity of the DI-water (η = 1.02 x 10^{-3} Pa s) at room temperature and *k* is the permeability of the material [m^2]. This estimation leads to a minimum diffusion time of 703 seconds up to a maximum time of 21420 seconds for Opalinus in this study. This means that the pore fluid was not fully equilibrated during all experiments, which should primarily affect the results of the shorter holds. Consequently, this variability might affect the amount of frictional healing depending on the healing mechanism. Additionally, the viscosity decreases for experiments with elevated temperatures, leading to lower diffusion times. The observed increase in frictional healing at higher temperatures (Figure 9a) suggests that the healing mechanism is related to the diffusion time.

Reproducibility of the experiments

The duplicate experiments in the RS give insight into the accuracy and reproducibility of the results. The measurement equipment has very high resolutions which makes the error of the apparatus neglectable compared to the reproducibility of the experiments. The main source of error therefore results from human error or sample variability which can lead to differing results. For instance, this occurs when the material is deposited between the confining rings with a slightly uneven distribution or due to the horizontal attachment to the upper piston block. An uneven distribution can consequently lead to slight tilting of the upper forcing block resulting in an unbalance between the two load cell measurements. This affects the results because the shear stress is consequently not fully measured perpendicular to the fault zone. Another reproducibility inaccuracy results from the apparatus design. After the experiments, different amounts of material was found in the piston which could be lost during various phases of the experiment. Firstly, different amounts of material can be lost because of the use of varying piston sets which have different confining rings and consequently different gaps. Secondly, material can escape during the preparation phase when attaching the piston set to the upper forcing block which is done horizontally or during lifting of the setup into the pressure vessel. Finally, the randomness of the grain size distribution which can escape the confining rings (Figure 3) can result in different material loss. This leads to varying gouge thicknesses or compositions between experiments, which subsequently affects the frictional behaviour. The thickness changes the strain rate which directly influences the frictional strength and a different composition leads changes the frictional strength of the material because phyllosilicates are weaker compared to feldspar and quartz, which is also found in SWy-2 (Chipera & Bish, 2001).

The two identical experiments enable the assessment and quantification of the minimum error in the RS experiments (Figure 15). These experiments demonstrate that the second SHS series has a significantly lower accuracy compared to the first series which can be the result of two factors. Firstly, the differing conditions between the two SHS series (The first series conducted with 50 MPa pore fluid pressure compared to 10 MPa in the second series) could suggest that a lower pore fluid pressure leads to less accurate results. This is because the lower pore fluid pressure also lowers the normal stress which results in larger apparent errors due to the lower peak strength. The other explanation could be that the second SHS series already has more total displacement, leading to inaccurate results. This could be the consequence of different amounts of material lost due to human reproducibility errors when preparing the sample, or from apparatus inaccuracy due to varying layer thicknesses. Comparing the creep relaxation results of the RS and DS (Figure 13b), a similar trend of larger errors with longer hold periods and lower pore fluid pressures is observed.

Another inconsistency is found in some experiments that deviate from the log linear trend described by Carpenter et al. (2016). Some experiments follow the log linear trend while other experiments show deviating curves with extreme positive or negative frictional healing from the log linear trend. Especially results from experiments u1196 until u1206 show a lot of inconsistent results at longer hold times so the focus will be on the shorter hold time results. After experiment u1210 when the seal of the RS was replaced, the consistency of results positively changed after the replacement of the seal in the RS (Figure 2b).

Comparison of the Ring shear and Direct shear apparatus.

In order to validate the results in the RS, additional DS experiments were performed on Opalinus clay and on smectite. Both DS experiments showed no significant frictional healing peaks during the SHS sequences. This was expected for the experiment on Opalinus clays because these were also not observed during the RS experiments. For smectite however, peaks were expected but absent, leaving the question if the measured peaks in the RS are material or apparatus-induced. To answer this question the results and apparatus characteristics which can influence this difference in friction behaviour will be discussed. The results of the RS experiment u1212b will be compared to the first SHS sequence of the smectite DS experiment because they have similar conditions. For Opalinus RS experiment u1206 will be compared to the DS experiment on Opalinus.

The shear stress of smectite in the RS of 3.6 to 4.2 MPa was almost a factor 2 higher than the 2.2 to 2.4 MPa in the DS. For the experiments on Opalinus clay, the shear stress was 16.65 to 22.46 in the RS and 12.4 to 12.7 MPa in the DS (Figure 7 and figure 12). The Opalinus clay experiments in the DS were performed with a lower effective normal stress compared to the RS. Therefore, these cannot be compared directly but only used for indications if they are in the same order. This higher effective normal stress can explain why a higher shear stress is observed in the RS. Comparing the creep relaxation (Figure 13) the results show that the Opalinus clay has a similar relaxation behaviour in the RS and DS. Smectite on the other hand has a significantly (up to 10 times) lower creep relaxation in the RS and during the shortest holds ($\Delta\mu$ = 0.001 vs 0.011). This difference in steady state friction and creep relaxation indicates that one of the experiments might not be representative and that the apparatus or preparation method has significant effects on the results.

Figure 16 presents the evolution of the friction coefficient of single (1000 seconds) SHS tests in the different apparatus. The graph indicates differences in creep relaxation between the DS and RS shear apparatus, as well as variations in the DS internal and external force measurements. Comparing the slopes upon resliding, different trends are observed. The RS exhibits a steep increase at resliding, which gradually decreases until peak friction. This trend is similar to the external DS measurement but with a less steep slope. The internal DS measurement also shows a different trend, with friction beginning with the flattest slope and only increasing after a small displacement. This suggests significant differences in the stiffness of the apparatus, which subsequently influence the calculated amount of healing.

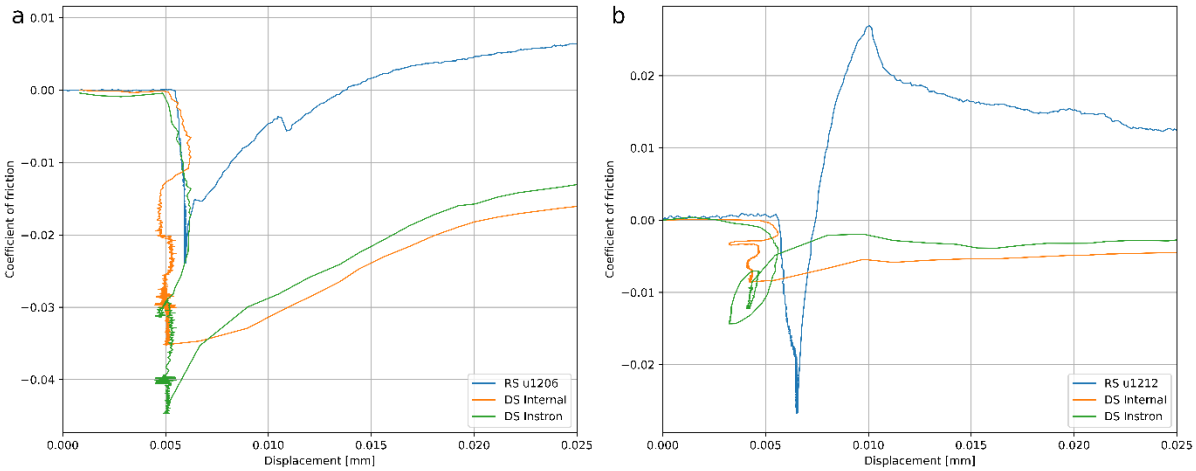

Figure 16: Relative coefficient of friction corrected to zero during the 1000-second hold for a) Opalinus clay and b) Smectite.

During the hold, the shear stress decreases because the loading is interrupted. However, the DS apparatus is never completely stationary and sometimes even seems to move back which results in a curving creep relaxation curve. In the DS, there is even an increase in friction measured on the external load cell. The apparent movement of the sample during the hold can have different origins. Firstly, the pore fluid pressure might vary internally because of the low permeability of the material. Also, elastic machine distortion, the seal, internal spacer or heat tubes which are between the sample and external measurement cell can all influence the measured displacement or force in the sample. This shows that the internal measurement is more representative for the actual force measurement because additional apparatus background is captured with the external measurement. Therefore, the internal measured data will be used for further discussion.

The difference in RS and DS results (Figure 12 and figure 13) can mean various things. Firstly, the measured peaks in the RS can be apparatus induced characteristics and are therefore not material properties. Before the seal was changed in the RS, a lower creep relaxation was observed on Opalinus clay (compared to the DS) with no frictional peaks during resliding. After replacing the seal, the smectite experiment in the RS showed more creep relaxation and also frictional peaks. This could suggest that Opalinus clay exhibits minimal or no healing behaviour compared to smectite. Alternatively, it is possible that the seal before or after the swap may have influenced the accuracy of the results. Considering that the RS experiment u1205 on smectite was done before the seal swap which also showed no frictional peaks, it would suggest that the seal has influenced the results. However, that still leaves the question if the smectite peaks are correct or whether the Opalinus clay results with no significant peaks are true. Additionally it is possible that the mineralogical difference or varying conditions between experiments lead to this difference. It is possible that most phyllosilicates in OPA are not swelling which is in line with the measurement of Corkum and Martin (2007) that only 10% consist of a mixture of illite-smectite. However, if both DS experiments on OPA and SWy-2 are correct it would imply that no peaks should be observed in the RS. On the other hand, several factors seem to influence the DS experiment resulting in irregular relaxation patterns during the hold period. Additionally, the grain size difference in the RS and DS could result in a different healing behaviour because with smaller grains, the diffusion of water into the interlayer spaces is faster. This means that faster diffusion took place in the RS and indicates that the diffusion has a relation to the healing mechanism.

An important control over the measured friction is a uniform and known pore fluid pressure. However, this highly varies in smectite because of the extremely low permeability of the material (Chu & Wang, 2023). The differences in sample sizes in the DS and RS therefore also contribute to less uniform conditions between the experiments, resulting in different measured frictions between the DS and RS. Only a few studies have been conducted with both DS and RS apparatus. Osano (1999) compared both methods but with slightly different setups compared to this study. The study of Osano (1999) found that the internal angle of friction in the RS is higher than in the DS setup. In the RS, the material gets squeezed to the outer edges which results in higher and less uniform recorded stresses in the RS. These findings of Osano (1999) are in line with the higher shear stress measured in the RS in this study. Using an atomic force microscope, Kosoglu et al. (2010) determined the coefficient of friction of wet SWy-2 to be $\mu = 0.20 \pm 0.03$. This is more similar to the result of experiment u1212b in the RS ($\mu = 0.14 - 0.17$) than the steady state friction in the DS ($\mu = 0.09 – 0.10$).

Additionally, previous studies found that the frictional strengthening and creep relaxation values obtained in SHS tests are a function of both the properties of the material but are also influenced by the stiffness of the apparatus used for the experiment (Beeler et al. 1994; Marone and Saffer 2015). Therefore we can compare the different experiments from the RS safely to the other RS experiments in this study. A variation in apparatus stiffness can explain differences in frictional healing values to other studies. For SHS tests, it is favourable that the apparatus has a high stiffness because this ensures that the load point velocity is close to the inelastic sliding velocity (Ferdowsi & Rubin, 2021). The peak strength is influenced by the stiffness of the apparatus, with a higher stiffness yielding larger values of Δμ during reloading because of a faster reloading response (Beeler et al., 1994). The RS apparatus has a higher stiffness compared to the DS apparatus so is expected to show more frictional healing. Additionally, a higher stiffness results in less creep relaxation, but the opposite is observed for smectite with RS results showing significantly higher creep relaxation compared to the DS (Figure 13). This could be a reason for the absence of frictional healing peaks in the DS.

Considering that the coefficient of friction results from the RS align more closely with literature findings (Kosoglu et al. 2010; Morrow et al. 2017) and that consistent trends were observed after the seal change, it is more probable that the RS smectite results after experiment u1210 are accurate. Moreover, during the holds of the Opalinus clay RS experiments sudden drops in shear stress were observed before the replacement of the seal and in one experiment an increase in shear stress was measured during the hold while no shearing was imposed on the sample. Therefore, the smectite experiments from the RS apparatus will be used for further discussion because they seem to have a better match with what we expect of the material from other literature.

Effect of material properties on frictional behaviour

Previous studies found that the frictional behaviour strongly depends on the phyllosilicate content in gouges, with frictionally weak materials showing lower rates of frictional healing an creep relaxation compared to frictionally stronger samples (Carpenter et al., 2016; Seyler et al., 2023).

The steady-state friction of the smectite experiments ranges between $\mu = 0.11$ and $\mu = 0.28$, with a mean of $\mu = 0.168$ (Table 3). This is low compared to the classical frictional strength proposed by (Byerlee, 1978) but consistent with previous studies on wet smectite (Kosoglu et al. 2010; Morrow et al. 2017; Niemeijer et al. in prep.). The low frictional strength of wet smectite is influenced by the weakly bound structure of water layers, which lubricate the material by separating the particles(Israelachvili et al., 1988). Consequently, wet smectite samples exhibit a significantly lower coefficient of friction compared to dry samples(Morrow et al. 1992; Morrow et al. 2017).

The observed creep relaxation during the hold period of SHS experiments is considered to be representative of afterslip of earthquakes (Marone et al. 1991). During the hold, strain energy from the sample and testing apparatus is converted to sample creep (slip) which results in reduced shear stress. The measured creep relaxation rates in this study ($\beta_c < 10x10^{-3}$ log(s^{-1})) are in line with low rates observed in other studies on smectite (Carpenter et al., 2016). Figure 17 shows the frictional healing and relaxation rates plotted against the values obtained by (Carpenter et al., 2016). These authors performed experiments on natural and synthetic fault gouges at room temperature with no pore fluid phase, but 100 % relative humidity of the sample. They found that the β and β_c rates scale with the steady state friction of different rock gouges. The frictional strong calcite-rich gouges plot on the right side of figure 17 ($\mu_{ss} > 0.6$), the quartz

and feldspar-rich gouge in the middle and phyllosilicate-rich samples on the left side of the figure (μ_{ss} < 0.33). The smectite results of this study plot with the low steady state friction phyllosilicate data from Carpenter et al. (2016), but for some experiments significantly higher β and β_c rates have been observed (Table 3). Although different conditions were used in this study, the higher rates indicate that specific conditions result in higher frictional healing of smectite compared to other phyllosilicate material. To investigate which healing mechanism could be responsible for increased healing rates in this study, the effect of different conditions on the frictional healing will be discussed.

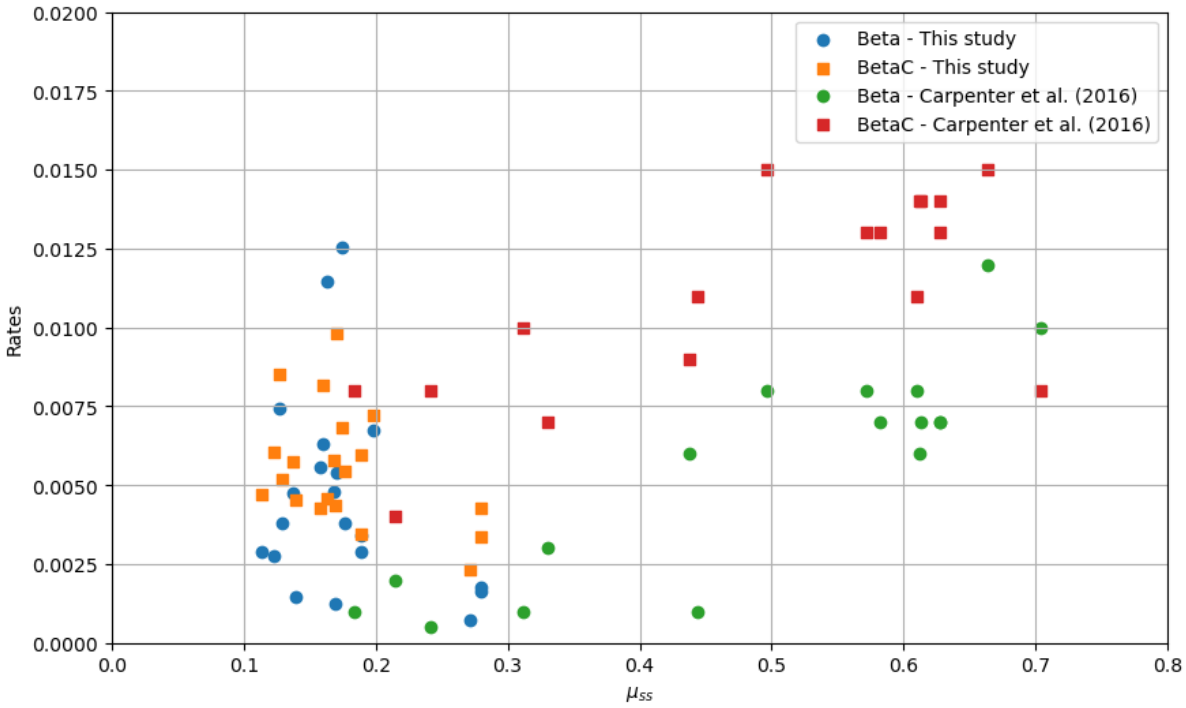

Figure 17 Frictional healing and creep relaxation rates of smectite compared to the study of (Carpenter et al., 2016).

Effect of temperature on friction, frictional healing, creep relaxation and RSF parameters

No systematic studies have been performed to investigate the temperature effect on the frictional strength of smectite, although some studies have examined smectite in combination with other minerals. (Boulton et al., 2014; Carpenter et al., 2016; Kubo & Katayama, 2015). Boulton et al. (2014) compared smectite-rich clay to illite/muscovite and found that smectite is approximately 30% weaker at room temperature while being stronger above 140 °C (Boulton et al., 2014). This indicates that smectite plays a crucial role in the temperature dependency of the gouge strength. Experiments by Kubo and Katayama (2015) on dry Ca-smectite at 60 MPa normal stress demonstrated that the steady-state friction increases with temperature from room temperature to 200 °C due to the dehydration of adsorbed water. Although this study is on wet smectite, a similar temperature effect is observed (Figure 7c) with the steady state friction at 120 °C being higher than at 80 and 20 °C.

Shibasaki et al. (2017) investigated the temperature dependency of smectite-rich soils on the frictional healing under conditions of slow shearing rates and low normal stresses. They found a positive temperature effect on the strength of the soil, consistent with the frictional healing results of this study. At 120 °C, more than double the peak sizes were measured compared to 20 °C (Figure 13). This trend is also found in the frictional strengthening rates (β) which are 12.52 x 10^{-3} log(s^{-1}) at 120 °C and only 4.73 x 10^{-3} log(s^{-1}) at room temperature (Table 3). These rates are

of the same order as previous research. For example, rates of $\beta = 2.5 \times 10^{-3}$ log(s^{-1}) have been documented on (40%) smectite fault gouge at 20 °C and a constant normal load of 1 MPa (Ikari et al., 2016). In contrast to the frictional healing, smectite creep relaxation does not show a temperature dependency with similar trends at different temperatures. The creep relaxation rates β_c = (2.3 to 9.8 x 10^{-3} log(s^{-1})) are slightly higher than reported in previous research (1.9 x 10 10^{-3} log(s^{-1})) on smectite containing gouge by Ikari et al. (2016). However, the rates are still in the same order and can indicate that smectite exhibits slightly higher creep relaxation rates compared to other clays, or this difference could be attributed to the stiffness of the apparatus.

Another study has documented that at 150 °C and 60 MPa, the velocity dependence of smectite changes from velocity-strengthening to velocity-weakening behaviour (Kubo & Katayama, 2015). Mizutani et al. (2017) also reported velocity weakening behaviour at lower temperature, but only with higher effective normal stresses (σ_n^{eff} > 50 MPa at 25 °C). They, however only calculated *a-b* values from velocity-step test which does not show the dependence of hold time as demonstrated in this study. Figure 10 indicates that the length of the holds influences the velocity dependence of smectite. Specifically, higher temperature result in a decrease in a-b values for holds longer than 100 seconds. Therefore, elevated temperatures lead to less velocity-strengthening behaviour compared to a lower temperatures. This will be discussed further in the context of the swelling behaviour.

Effect of effective normal stress on friction, frictional healing, creep relaxation and RSF parameters

The experiments in this study indicate that a lower effective normal stress results in more frictional healing compared to higher stresses (Figure 9c). For experiment u1223 and u1224 (σ_n = 37.5 and 62.5), the frictional healing decreased at longer hold periods (t_{hold} > 1000 s), which is opposite to the general trends found in other studies where frictional healing typically increases with hold time (Marone and Saffer 2015). The creep relaxation also deviates after holds of 1000 s from the expected trend. This is an indication of reproducibility errors and therefore only the shorter hold will be used for further discussion.

In this study, it is demonstrated that higher effective normal stress results in a higher steady state shear stress (Figure 7b/c), consistent with Byerlee's rule (Byerlee, 1978). As a consequence of a higher effective normal stress, water inside the smectite structure is forced out, decreasing the ability to facilitate sliding which leads to increased shear stress (Moore & Lockner, 2004). However, this trend has not been found for smectite in this study which is demonstrated by the friction coefficient (Table 3). Morrow et al. (2017) observed a decrease in the steady state friction coefficient (μ_{ss}) with elevated effective normal stress. The experiments of Morrow et al. (2017) however were conducted at room temperature, with a sliding velocity of 0.1 µm/s and performed with a broader range of effective normal stresses (10 to 600 MPa) compared to this study (Figure 7). This indicates that elevated temperatures might influence this relationship. An opposite effect has been observed by Mizutani et al. (2017), whereby only an increase was found with effective normal stress conditions of $\sigma_n^{eff} \geq 30$ MPa. Furthermore, the study of Saffer et al. (2012) with effective stresses up to 155 MPa also did not find a relationship of the effective normal stress and steady state friction coefficient. These differing results among studies indicates that other conditions such as the temperature and pore fluid pressure might influence this relationship, or the changes in friction are not significant within the smaller stress range in this study. Additionally, the effect of the seal friction is more significant for low effective normal stresses which could result in the absence of a clear trend.

The creep relaxation results demonstrates a trend where a higher effective normal stress leads to less creep relaxation during the hold phases. For example, there is double the amount of creep relaxation (difference of $\mu_c = 0.01$ for $t_{hold} = 10$ s up to $\mu_c = 0.02$ for $t_{hold} = 10000$ s) for experiment on an effective normal stress of 25 MPa compared to the experiment on 75 MPa (Figure 9d). These trends are also defined in the frictional strengthening ($\beta = 12.53 \times 10^{-3}$ log(s^{-1}) for 25 MPa and $\beta = 3.81 \times 10^{-3}$ log(s^{-1}) for 75 MPa) and creep relaxation rates ($\beta_c = 6.82 \times 10^{-3}$ log(s^{-1}) for 25 MPa and $\beta_c = 5.44 \times 10^{-3}$ log(s^{-1}) for 75 MPa), although they are less pronounced because of the high value for the constant *c* in equation 5 which is neglected in all studies (Table 3). However, future studies on this constant could possibly reveal interesting trends which might depend on the type of healing mechanism.

Mizutani et al. (2017) conducted research on the RSF parameters of smectite and found that dependence of *a-b* on the effective normal stress changes from negative at low temperatures (25 °C) to flat at high temperatures (150 °C). The effective normal stress dependence has been studied with a temperature of 120 °C in this study, this trend may change with a lower temperature as Mizutani et al. (2017) revealed. However, the effective normal stress does not seem to influence the *a-b* values with the conditions in this study (Figure 10).

Effect of pore fluid pressure on friction, frictional healing, creep relaxation and RSF parameters

The pore fluid pressure was adjusted after the first SHS sequence during all experiments. For the smectite experiments from u1212, the pore fluid pressure was reduced from 50 to 10 MPa. As the Instron controlled the effective normal stress, this adjustment in pore fluid pressure subsequently led to a decrease in the normal stress due to the effective normal stress being held constant between these two SHS series. A slight increase in steady state shear stress was observed with a lower pore fluid pressure but this is more apparent for experiments with higher effective normal stresses (Figure 7). This can be a result from the seal friction which are less significant with higher stress levels. Additionally, the minimum error of the experiment increases with more total displacement for the second SHS sequences on 10 MPa (Figure 15).

The results from the effect of pore fluid pressure on the frictional healing indicate that the healing increases with pore fluid pressure (Figure 9) until 50 MPa for short holds ($t_{hold} < 1000$s). At 100 MPa pore fluid pressure, less frictional healing is measured than at 50 MPa. This indicates that there could be a maximum frictional healing between 10 and 100 MPa pore fluid pressure. However, the experiment at 100 MPa was the second SHS sequence, which has a lower accuracy as described earlier. This makes it plausible that there is only an overall trend with higher pore fluid pressures resulting in more frictional healing. Furthermore, an increasing trend is also observed in the relationship between the pore fluid pressure and creep relaxation. Additionally, the RSF results for short hold periods ($t_{hold} < 1 \times 10^4$ s) indicate that higher pore fluid pressures lead to increasing *a-b* values, implying more velocity strengthening behaviour with higher pore fluid pressures. This correlation is also systematically visible for only *a* values which are higher at elevated pore fluid pressures (Figure 11).

Although different studies have been performed on comparing dry and wet smectite, no study has investigated the effect of pore fluid pressure on the frictional strength of smectite with demineralised water as the pore fluid phase. The study of Seyler et al. (2023) suggests that saturation of clays reduces the real contact area of clays, leading to lower healing rates. This makes clay-rich materials weaker with less restrengthening during the holds. Other authors have observed that higher pore fluid pressure leads to an increase in fluid which can be incorporated into the structure of the material (Di Maio et al., 2004). According to the findings of Seyler et al. (2023), this trend should result in lower healing rates. However, the opposite is

observed in this study indicating that smectite exhibits more healing compared to other phyllosilicates under increased pore fluid pressure conditions.

Swelling behaviour of smectite

Smectite is known for its high swelling behaviour due to the sorption interaction with water (Saiyouri et al., 2004). The effects of different conditions on the swelling behaviour will be discussed in order to investigate if sorption is responsible for the increased healing of smectite compared to other phyllosilicates which has been observed in this study (Figure 17). The sorption capacity and thus amount of swelling can be influenced by different conditions (Akinwunmi et al., 2019), but another factor controlling this process is the ease in which water can enter the interlayer spaces. Sorption itself is quite time-independent, making the diffusion speed a controlling factor over this process. The permeability and viscosity of the water have an important control over the diffusion speed.

Different studies have been conducted on the effect of temperature on the swelling behaviour of smectite. Both increasing and decreasing effects have been found which can be explained by different factors such as varying clay types, different experimental conditions or types of exchangeable cations (Yang et al., 2021). The increased smectite healing observed in this study compared to other clay-rich gouges from other studies (Figure 17) can indicate that sorption is the dominant healing mechanism in smectite because of the high swelling potential of smectite. Studies on the swelling behaviour of Na-smectite under similar temperature conditions (up to 150°C) to this study, indicate a positive correlation between temperature and amount of swelling (Akinwunmi et al., 2019; Morodome & Kawamura, 2009). This is also in line with increased frictional healing observed in this study with elevated temperatures. With a higher temperature, the kinetic energy of water is increased, leading to a lower viscosity of the fluid. Consequently, water can more easily enter into the interlayer spaces resulting in faster swelling and possibly the ability to enter smaller pores resulting in more sorption.

The RSF results from this study indicate that higher temperatures lead to less frictional strengthening after holds of 100 seconds. If sorption depends on the speed at which fluid can move around in the clay particle, it should be reflected in the *b* parameter, which describes the evolution effect in the RSF equation (Equation 1). While the direct parameter *a* remains fairly constant, except for the shorter holds where slightly higher *a* values are captured for 120 °C (Figure 11). The *b* parameters on the other hand are significantly higher for the elevated temperatures, especially for the longer hold periods. This indicates that the evolutionary effect is more dominant for longer holds at higher temperatures, confirming the importance of the evolutionary effect on the healing.

Studies on the swelling behaviour as a result of different stress levels indicated that the sorption capacity of clays decreases with increased normal effective stress (Zhang 2019). Consequently, this decrease in sorption leads to a reduction in frictional healing which is consistent with the results of this study. Also, an increase in effective normal stress results in a decrease in permeability. During sliding water is pushed out of the structure and is not able to enter the interlayer spaces quickly. With a lower permeability, water is slower in re-entering the pores and interlayers structure, resulting in a slower sorption effect. This is in line with the decrease in frictional healing observed under high effective normal stresses.

The study of Morrow et al. (2017) on wet smectite at room temperature found an increase of *a-b* values with higher effective normal stress. However, this relationship was not observed in the RSF friction values in this study which showed no significant relationship with the effective

normal stress and only a dependence on the hold time (Figure 10). However, both the *a* and *b* parameters individually appear to be dependent on the effective normal stress (Figure 11). For example, the b parameter is higher for lower effective normal stresses, indicating that the evolution effect is more dominant under these conditions. This aligns with the decrease in swelling behaviour as a result of increasing effective normal stress (Zhang 2019).

Finally, the effect of pore fluid pressure on the frictional healing also seems to be in line with expected swelling behaviour. Literature on the behaviour of clays under various pore fluid pressures indicates a positive correlation between pore fluid pressure and swelling (Ghalamzan et al., 2022). With a higher pore fluid pressure the capillary force is increased which is necessary for a fluid to squeeze through a pore throat (Vavra et al., 1992). This consequently results in faster and more swelling of the smectite because more interlayer spaces can be filled with water at a higher rate leading to more healing. This is consistent with the results of this study which show more frictional healing with higher pore fluid pressures. The RSF *a* values of the elevated pore fluid pressures (50 and 100 MPa) are higher for the short holds and decrease for longer holds. Additionally, the *b* values of experiments with elevated pore fluid pressures increase with the hold time (Figure 11). This indicates that the evolutionary effect becomes more important with the hold time which is also in line with swelling as dominant healing mechanism.

The observed effects of different conditions align with the expected swelling behaviour, indicating that sorption is likely the dominant healing mechanism for smectite-rich clay gouges. Consequently the question arises how the swelling is able to promote frictional healing. One possibility is that increased sorption replaces weaker interlayer bonds with stronger water bonds, resulting in a stronger material. This could lead to a peak in friction upon resliding, reflecting the stronger bonded material.

Another explanation I propose is that the volumetric increase of particles disrupts the "smooth" sliding fault surface by forming smectite bulges along the fault plane. Figure 18 shows microscopic observations and schematic drawings of a phyllosilicate microstructure of sheared gouge from den Hartog et al. (2020). Figure 18A shows the situation during sliding, a “smooth” sliding surface is created with water facilitating shear along the fault plane. The water is pushed out of the interlayer spaces and is collected in bigger pores. During the hold, water is able to re-enter the interlayer spaces resulting in a volumetric increase of the clay particles. Consequently, these particles disrupt the “smooth” fault surface (Figure 18D) which increases the material strength and promotes healing. Upon resliding, the disturbed surface or a completely new fault plane needs to be established, leading to peak friction followed by subsequent weakening with further shearing.

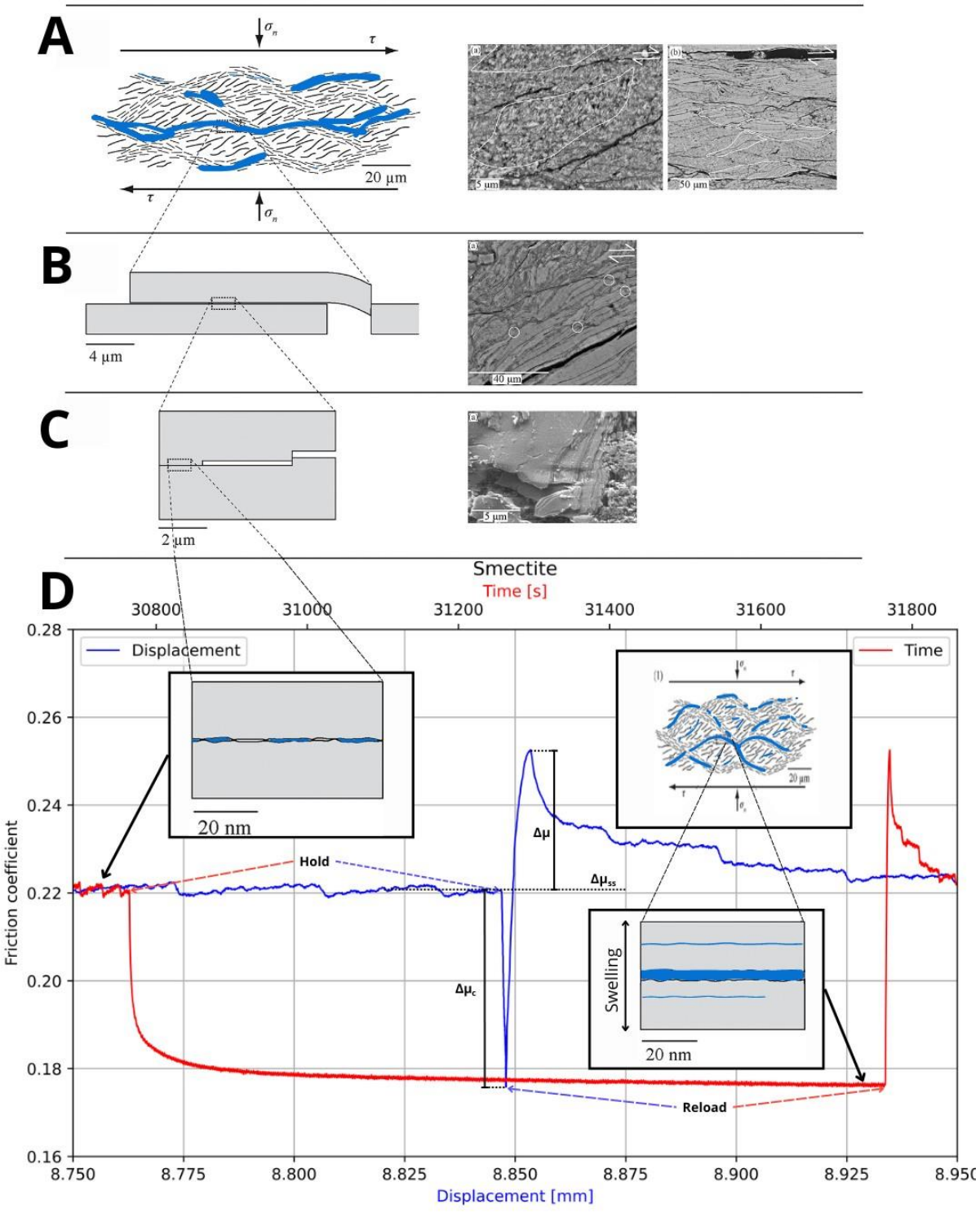

Figure 18: Microscopic observations and schematic drawings (from den Hartog et al. (2020) of a phyllosilicate microstructure with added interpretations during shearing and holding phases of a SHS series. The magnification is increased from A to D. During the hold, the smooth sliding surface is disrupted due to the swelling of independent clay particles.

The swelling speed is highest during the initial phase when water is introduced to a swelling clay and then gradually decreases until the maximum sorption capacity is reached (Zhang et al. 2018). In this study, water is already introduced to smectite but pushed out of the smectite

structure during sliding and will re-enter the interlayer spaced during the hold. Therefore, it is expected that faster swelling rates occur at the beginning of the hold and then gradually decrease until the maximum capacity is reached. This is consistent with the log-linear trend observed, whereby the healing rate decreases over time due to decreasing swelling speed. This raises the question for how long the swelling and consequently healing will continue. If there is a maximum sorption capacity the amount of healing from swelling should reach a peak value. The maximum frictional strengthening rate observed in this study was $\beta = 12.53 \times 10^{-3}$ log(s^{-1}) with a maximum healing of $\Delta\mu = 0.045$ after 30000 seconds. If we assume frictional healing will continue at that rate, the amount of healing after 10 years would be $\Delta\mu = 0.1$ and after 1 million years $\Delta\mu = 0.17$. These increases are significant for smectite with a steady state friction of approximately $\mu_{ss} = 0.20$. The Ten Boer claystone, containing phyllosilicates has a frictional strength of $\mu = 0.4$ compared to $\mu = 0.6$ for the Slochteren sandstone reservoirs (Hunfeld et al., 2020) in which the earthquakes in the Groningen gas field nucleate. Understanding how formations containing smectite (such as the Ten Boer claystone) can restrengthen is crucial, as previous research found that frictional strengthening is necessary for repeated earthquake failure (Marone and Saffer 2015). Therefore, further research is needed on materials containing less smectite to investigate if these formation can significantly restrengthen as has been found in this study.

Implications and future research

From studying the effect of different conditions on the frictional healing, some implications for the stability of the subsurface containing smectite-rich clays can be made. For the Groningen gas field, extraction decreases the pore fluid pressure which will increase the effective normal stress. The results from this study determined that this negatively effects the frictional healing which leads to less strengthening during the inter-seismic period. The velocity dependence also plays a crucial role in earthquake behaviour (Dieterich 1979; Marone 1998). Although smectite only exhibited velocity strengthening behaviour, a decrease in pore fluid pressure leads to less velocity strengthening. This is important because less strengthening increases the chance of earthquakes rupturing further into the smectite-rich layers. In literature, negative a-b values for clay mixtures containing smectite have been reported (Mizutani et al. 2017; Morrow et al. 2017; Niemeijer et al. in prep.), indicating that the trends observed in this study might be extrapolated to velocity weakening behaviour for longer hold times. This could potentially lead to further earthquake rupture in the Ten Boer claystone.

The permeability of smectite is too low for geothermal exploration. However, if these layers are situated close to reservoirs utilized for geothermal exploration, the temperature can still decrease. This reduction in temperature will decrease the frictional strengthening of the material which subsequently can host less heavy earthquakes. Moreover, the temperature also has a negative effect on the *a-b* values for longer hold times (t_{hold} >100 s), promoting velocity strengthening behaviour. As a result there is a reduced chance of earthquake nucleation or rupture. Therefore, with geothermal exploration, the seismic risks of adjacent smectite-rich layers declines.

Future research can enhance our understanding of the healing mechanisms of smectite-rich clays further by measuring the expansion of the material during a SHS cycle. In this study, dilatancy was not measurable due to the small sample size and material loss during the experiment. Using larger sample sizes and confining rings that fully seal the material enable the possibility to research the dilatancy effect. Furthermore, the effects of different pore fluid pressures and effective normal stresses on the frictional healing were studied at a temperature

of 120 °C. Results determined the significance of temperature on the frictional healing so it would be interesting to see if the trends are also observed at lower temperatures. Other studies can also focus on mixtures with other minerals to simulate smectite bearing layers which are found close to the Groningen gas field. Another uncertainty in this study is the duration and capacity of swelling. Experiments with longer hold times will give crucial information about the maximum sorption capacity of smectite. Finally, to add to the understanding of the healing mechanisms in smectite, microstructural analysis can be performed on sheared material. This can reveal details about the particle alignment, texture and shearing surface, providing crucial information about the possible healing mechanisms and behaviour of the fault zone.

Conclusion

In this study, I performed SHS experiments in a hydrothermal RS apparatus on Opalinus claystone and smectite, with sliding at 1 µm/s and holds ranging from 3 to 30000 seconds. Experimental conditions were varied with temperatures of 20 to 120 °C, effective normal stresses of 25 up to 75 MPa and pore fluid pressures ranging from 1 to 100 MPa. The aim of this study is to enhance our understanding of time-dependent healing mechanism of clay-rich fault gouge by investigating the effects of variable temperature, pore fluid pressure and effective normal stress on the amount and rate of healing. Results from this study demonstrate that different material compositions significantly impact the healing behaviour of the materials. While Opalinus claystone exhibited no significant frictional healing ($\Delta\mu < 0.005$) within the conditions and time-scope of this study, smectite on the other hand showed significant healing ($\Delta\mu$ up to 0.05) with frictional strengthening rates ranging from 1.25 to 12.53 x 10^{-3} log(s^{-1}).

The varying experimental conditions revealed that increased temperature and pore fluid pressure enhance the amount of healing, whereas an opposite effect was found for the effective normal stress. Additionally, temperature did not influence the creep relaxation, whereas higher effective normal stress resulted in less creep relaxation. The opposite was observed for the pore fluid pressure, showing a positive correlation with the creep relaxation. These findings are in line with the behaviour of water and how easily it is able to move around and enter the interlayer space of smectite. This suggests that sorption is the dominant healing mechanism in smectite-rich clay gouge.

Based on these findings, I propose that the increased frictional healing resulting from increased sorption is due to the volumetric expansion of the particles. This volume increase disrupts the “smooth” sliding plane by forming bulges of smectite over the fault plane, leading to an increased strength of the sample. Upon sliding, a new or smooth plane needs to be created, resulting in a peak friction and subsequent weakening. As an alternative to this explanation, it is possible that more interlayer spaces are filled with water. This increased sorption leads to stronger bonds between the phyllosilicate sheets compared to the original weaker interlayer bonds without adsorbed water.

Additionally, this study revealed that the RSF velocity dependence of smectite not only changes with varying conditions but also with the length of the hold times. An elevated temperature has a negative effect on the velocity-strengthening behaviour of smectite for holds longer than 1 x 10^2 s, while the pore fluid promotes velocity-strengthening behaviour for holds shorter than 1 x 10^4 s. These findings suggest that the effect of smectite in the clay-rich layers in the Groningen gas field reduces frictional healing with decreasing pore fluid pressure and increasing effective normal stress. Finally, the RSF analyses indicate a higher potential for earthquake nucleation or propagation under these conditions due to reduced velocity-strengthening behaviour.

Further research should include microstructural analysis on sheared smectite-rich clay gouge in order to investigate indications of the healing mechanism by studying the sliding plane and examining for instance the particle alignment, texture and grain sizes. Additionally, the effect of compaction (and dilatancy) can be studied by measuring the material thickness during a SHS test, which should give an indication for the sorption behaviour. Finally, new research can explore extended ranges of conditions, hold times or sample sizes to investigate how this behaviour scales to the larger natural dimensions and longer timescales. Also, choosing natural materials such as the Ten Boer claystone from Groningen would help link the results to nature.

Acknowledgement

I would like to thank my supervisors dr. André Niemeijer and Mike Sep for their guidance throughout my thesis. André provided interesting discussions and gave very helpful tips guiding me through my project. Mike always offered good insights for my thesis, helped me with the direct shear experiments and was fun to hang around with in the ESL. Also, this study could not have been completed without the technicians from the HPT lab. They helped with fixing problems with the ring, direct shear and other apparatus. I also thank Chien-Cheng for taking the time to explain the direct shear setup while in the busiest time of his PhD. Furthermore, I would like to thank the people working in the ESL for creating a nice working environment, especially Sandra for the serious and less serious discussions throughout my thesis. Finally, this research was made possible by the DeepNL program.

References

Akinwunmi, B., Sun, L., Hirvi, J. T., Kasa, S., & Pakkanen, T. A. (2019). Influence of temperature on the swelling pressure of bentonite clay. *Chemical Physics*, *516*, 177–181. https://doi.org/10.1016/j.chemphys.2018.09.009

Bakker, E. (2017, February 22). *Frictional and transport properties of simulated faults in CO2 storage reservoirs and clay-rich caprocks* [Dissertation]. UU Dept. of Earth Sciences. https://dspace.library.uu.nl/handle/1874/347158

Bakker, E., & de Bresser, J. H. P. (2020). Anisotropic transport and frictional properties of simulated clay-rich fault gouges. *Solid Earth Discussions*, 1–25. https://doi.org/10.5194/se-2020-178

Beeler, N. M., Tullis, T. E., & Weeks, J. D. (1994). The roles of time and displacement in the evolution effect in rock friction. *Geophysical Research Letters*, *21*(18), 1987–1990. https://doi.org/10.1029/94GL01599

Boulton, C., Moore, D. E., Lockner, D. A., Toy, V. G., Townend, J., & Sutherland, R. (2014). Frictional properties of exhumed fault gouges in DFDP-1 cores, Alpine Fault, New Zealand. *Geophysical Research Letters*, *41*(2), 356–362. https://doi.org/10.1002/2013GL058236

Buijze, L., van den Bogert, P. a. J., Wassing, B. B. T., & Orlic, B. (2019). Nucleation and Arrest of Dynamic Rupture Induced by Reservoir Depletion. *Journal of Geophysical Research: Solid Earth*, *124*(4), 3620–3645. https://doi.org/10.1029/2018JB016941

Byerlee, J. (1978). Friction of Rocks. In J. D. Byerlee & M. Wyss (Eds.), *Rock Friction and Earthquake Prediction* (pp. 615–626). Birkhäuser. https://doi.org/10.1007/978-3-0348-7182-2_4

Carpenter, B. M., Ikari, M. J., & Marone, C. (2016). Laboratory observations of time-dependent frictional strengthening and stress relaxation in natural and synthetic fault gouges. *Journal of Geophysical Research: Solid Earth*, *121*(2), 1183–1201. https://doi.org/10.1002/2015JB012136

Chipera, S. J., & Bish, D. L. (2001). Baseline Studies of the Clay Minerals Society Source Clays: Powder X-Ray Diffraction Analyses. *Clays and Clay Minerals*, *49*(5), 398–409. https://doi.org/10.1346/CCMN.2001.0490507

Chorom, M., & Rengasamy, P. (1996). Effect of Heating on Swelling and Dispersion of Different Cationic Forms of a Smectite. *Clays and Clay Minerals*, *44*, 783–790. https://doi.org/10.1346/CCMN.1996.0440609

Chu, C.-L., & Wang, C.-Y. (2023). Pore Pressure in Montmorillonite During Frictional Sliding. *Journal of Geophysical Research: Solid Earth*, *128*(11), e2023JB027601. https://doi.org/10.1029/2023JB027601

Clay Minerals Society. (n.d.). Source Clays Repository. Retrieved from https://www.clays.org/repository/

Corkum, A. G., & Martin, C. D. (2007). The mechanical behaviour of weak mudstone (Opalinus Clay) at low stresses. *International Journal of Rock Mechanics and Mining Sciences*, *44*(2), 196–209. https://doi.org/10.1016/j.ijrmms.2006.06.004

den Hartog, S., Faulkner, D., & Spiers, C. (2020). Low Friction Coefficient of Phyllosilicate Fault Gouges and the Effect of Humidity: Insights From a New Microphysical Model. *Journal of Geophysical Research: Solid Earth*, *125*. https://doi.org/10.1029/2019JB018683

Di Maio, C., Santoli, L., & Schiavone, P. (2004). Volume change behaviour of clays: The influence of mineral composition, pore fluid composition and stress state. *Mechanics of Materials*, *36*(5), 435–451. https://doi.org/10.1016/S0167-6636(03)00070-X

Dieterich, J. H. (1979). Modeling of rock friction: 1. Experimental results and constitutive equations. *Journal of Geophysical Research: Solid Earth*, *84*(B5), 2161–2168. https://doi.org/10.1029/JB084iB05p02161

Domenico, P. A., & Mifflin, M. D. (1965). Water from low-permeability sediments and land subsidence. *Water Resources Research*, *1*(4), 563–576. https://doi.org/10.1029/WR001i004p00563

Dost, B., Goutbeek, F., Eck, T., & Kraaijpoel, D. (2012). *Monitoring induced seismicity in the North of the Netherlands: Status report 2010*.

Emmerich, K. (2013). Chapter 2.13—Full Characterization of Smectites. In F. Bergaya & G. Lagaly (Eds.), *Developments in Clay Science* (Vol. 5, pp. 381–404). Elsevier. https://doi.org/10.1016/B978-0-08-098259-5.00015-9

Ferdowsi, B., & Rubin, A. M. (2021). Slide-Hold-Slide Protocols and Frictional Healing in Discrete Element Method (DEM) Simulations of Granular Fault Gouge. *Journal of Geophysical Research: Solid Earth*, *126*(12), e2021JB022125. https://doi.org/10.1029/2021JB022125

Földvári, M. (2011). *Handbook of thermogravimetric system of minerals and its use in geological practice*. Geological Inst. of Hungary.

Ghalamzan, F., De Rosa, J., Gajo, A., & Di Maio, C. (2022). Swelling and swelling pressure of a clayey soil: Experimental data, model simulations and effects on slope stability. *Engineering Geology*, *297*, 106512. https://doi.org/10.1016/j.enggeo.2021.106512

Hillers, G., Carlson, J. M., & Archuleta, R. J. (2009). Seismicity in a model governed by competing frictional weakening and healing mechanisms. *Geophysical Journal International*, *178*(3), 1363–1383. https://doi.org/10.1111/j.1365-246X.2009.04217.x

Hunfeld, L. B., Chen, J., Hol, S., Niemeijer, A. R., & Spiers, C. J. (2020). Healing Behavior of Simulated Fault Gouges From the Groningen Gas Field and Implications for Induced Fault Reactivation. *Journal of Geophysical Research: Solid Earth*, *125*(7), e2019JB018790. https://doi.org/10.1029/2019JB018790

Ikari, M. J., Carpenter, B. M., Vogt, C., & Kopf, A. J. (2016). Elevated time-dependent strengthening rates observed in San Andreas Fault drilling samples. *Earth and Planetary Science Letters*, *450*, 164–172. https://doi.org/10.1016/j.epsl.2016.06.036

Ikari, M. J., Saffer, D. M., & Marone, C. (2009). Frictional and hydrologic properties of clay-rich fault gouge. *Journal of Geophysical Research: Solid Earth*, *114*(B5). https://doi.org/10.1029/2008JB006089

Israelachvili, J. N., McGuiggan, P. M., & Homola, A. M. (1988). Dynamic Properties of Molecularly Thin Liquid Films. *Science*, *240*(4849), 189–191. https://doi.org/10.1126/science.240.4849.189

Karner, S. L., & Marone, C. (1998). The effect of shear load on frictional healing in simulated fault gouge. *Geophysical Research Letters*, *25*(24), 4561–4564. https://doi.org/10.1029/1998GL900182

Kosoglu, L. M., Bickmore, B. R., Filz, G. M., & Madden, A. S. (2010). Atomic Force Microscopy Method for Measuring Smectite Coefficients of Friction. *Clays and Clay Minerals*, *58*(6), 813–820. https://doi.org/10.1346/CCMN.2010.0580609

Kubo, T., & Katayama, I. (2015). Effect of temperature on the frictional behavior of smectite and illite. *Journal of Mineralogical and Petrological Sciences*, *110*(6), 293–299. https://doi.org/10.2465/jmps.150421

Marone, C. (1998). The effect of loading rate on static friction and the rate of fault healing during the earthquake cycle. *Nature*, *391*(6662), Article 6662. https://doi.org/10.1038/34157

Marone, C. J., Scholtz, C. H., & Bilham, R. (1991). On the mechanics of earthquake afterslip. *Journal of Geophysical Research: Solid Earth*, *96*(B5), 8441–8452. https://doi.org/10.1029/91JB00275

Marone, C., & Saffer, D. M. (2015). 4.05—The Mechanics of Frictional Healing and Slip Instability During the Seismic Cycle. In G. Schubert (Ed.), *Treatise on Geophysics (Second Edition)* (pp. 111–138). Elsevier. https://doi.org/10.1016/B978-0-444-53802-4.00092-0

McLaskey, G. C., Thomas, A. M., Glaser, S. D., & Nadeau, R. M. (2012). Fault healing promotes high-frequency earthquakes in laboratory experiments and on natural faults. *Nature*, *491*(7422), Article 7422. https://doi.org/10.1038/nature11512

Mizutani, T., Hirauchi, K., Lin, W., & Sawai, M. (2017). Depth dependence of the frictional behavior of montmorillonite fault gouge: Implications for seismicity along a décollement zone. *Geophysical Research Letters*, *44*(11), 5383–5390. https://doi.org/10.1002/2017GL073465

Moore, D. E., & Lockner, D. A. (2004). Crystallographic controls on the frictional behavior of dry and water-saturated sheet structure minerals. *Journal of Geophysical Research: Solid Earth*, *109*(B3). https://doi.org/10.1029/2003JB002582

Moore, D. E., & Lockner, D. A. (2007). 11. Friction of the Smectite Clay Montmorillonite: A Review and Interpretation of Data. In *11. Friction of the Smectite Clay Montmorillonite: A Review and Interpretation of Data* (pp. 317–345). Columbia University Press. https://doi.org/10.7312/dixo13866-011

Morodome, S., & Kawamura, K. (2009). Swelling behavior of Na- and Ca-montmorillonite up to 150°C by in situ X-Ray diffraction experiments. *Clays and Clay Minerals*, *57*(2), 150–160. https://doi.org/10.1346/CCMN.2009.0570202

Morrow, C. A., Moore, D. E., & Lockner, D. A. (2017). Frictional strength of wet and dry montmorillonite. *Journal of Geophysical Research: Solid Earth*, *122*(5), 3392–3409. https://doi.org/10.1002/2016JB013658

Morrow, C., Radney, B., & Byerlee, J. (1992). Chapter 3 Frictional Strength and the Effective Pressure Law of Montmorillonite and lllite Clays. In B. Evans & T. Wong (Eds.), *International Geophysics* (Vol. 51, pp. 69–88). Academic Press. https://doi.org/10.1016/S0074-6142(08)62815-6

Niemeijer, A. R., Spiers, C. J., & Peach, C. J. (2008). Frictional behaviour of simulated quartz fault gouges under hydrothermal conditions: Results from ultra-high strain rotary shear experiments. *Tectonophysics*, *460*(1), 288–303. https://doi.org/10.1016/j.tecto.2008.09.003

Niemeijer, A.R., Boulton, C., Amiri, H., & Plumper, O. (in preparation). Mixed-mode deformation of experimentally sheared calcite-smectite mixture under shallow subduction zone conditions. Manuscript in preparation, Department of Earth Sciences, Utrecht University, The Netherlands; Victoria University of Wellington, New Zealand.

Osano, S. N. (1999). *Direct Shear Box And Ring Shear Test Comparison: Why Internal Angle Of Friction Vary*. http://erepository.uonbi.ac.ke/handle/11295/39855

Penn State Rock and Sediment Mechanics Group. (2014). Xlook. GitHub. https://github.com/PennStateRockandSedimentMechanics/xlook

Rabinowicz, E. (1956). Stick and Slip. *Scientific American*, *194*(5), 109–119.

Ruina, A. (1983). Slip instability and state variable friction laws. *Journal of Geophysical Research: Solid Earth*, *88*(B12), 10359–10370. https://doi.org/10.1029/JB088iB12p10359

Saffer, D. M., Lockner, D. A., & McKiernan, A. (2012). Effects of smectite to illite transformation on the frictional strength and sliding stability of intact marine mudstones. *Geophysical Research Letters*, *39*(11). https://doi.org/10.1029/2012GL051761

Saffer, D. M., & Marone, C. (2003). Comparison of smectite- and illite-rich gouge frictional properties: Application to the updip limit of the seismogenic zone along subduction megathrusts. *Earth and Planetary Science Letters*, *215*(1), 219–235. https://doi.org/10.1016/S0012-821X(03)00424-2

Saiyouri, N., Tessier, D., & Hicher, P. Y. (2004). Experimental study of swelling in unsaturated compacted clays. *Clay Minerals*, *39*(4), 469–479. https://doi.org/10.1180/0009855043940148

Seyler, C. E., Shreedharan, S., Saffer, D. M., & Marone, C. (2023). The Role of Clay in Limiting Frictional Healing in Fault Gouges. *Geophysical Research Letters*, *50*(20), e2023GL104984. https://doi.org/10.1029/2023GL104984

Shibasaki, T., Matsuura, S., & Hasegawa, Y. (2017). Temperature-dependent residual shear strength characteristics of smectite-bearing landslide soils. *Journal of Geophysical Research: Solid Earth*, *122*(2), 1449–1469. https://doi.org/10.1002/2016JB013241

Smith, S. A. F., Nielsen, S., & Di Toro, G. (2015). Strain localization and the onset of dynamic weakening in calcite fault gouge. *Earth and Planetary Science Letters*, *413*, 25–36. https://doi.org/10.1016/j.epsl.2014.12.043

Tao, K., & Dang, W. (2023). Frictional behavior of quartz gouge during slide-hold-slide considering normal stress oscillation. *International Journal of Coal Science & Technology*, *10*(1), 34. https://doi.org/10.1007/s40789-023-00592-7

Tesei, T., Collettini, C., Carpenter, B. M., Viti, C., & Marone, C. (2012). Frictional strength and healing behavior of phyllosilicate-rich faults. *Journal of Geophysical Research: Solid Earth*, *117*(B9). https://doi.org/10.1029/2012JB009204

Van Eijs, R. M. H. E., Mulders, F. M. M., Nepveu, M., Kenter, C. J., & Scheffers, B. C. (2006). Correlation between hydrocarbon reservoir properties and induced seismicity in the Netherlands. *Engineering Geology*, *84*(3), 99–111. https://doi.org/10.1016/j.enggeo.2006.01.002

Vavra, C. L., Kaldi, J. G., & Sneider, R. M. (1992). Geological Applications of Capillary Pressure: A Review1. *AAPG Bulletin*, *76*(6), 840–850. https://doi.org/10.1306/BDFF88F8-1718-11D7-8645000102C1865D

Verberne, B. A., de Bresser, J. H. P., Niemeijer, A. R., Spiers, C. J., de Winter, D. A. M., & Plümper, O. (2013). Nanocrystalline slip zones in calcite fault gouge show intense crystallographic preferred orientation: Crystal plasticity at sub-seismic slip rates at 18–150 °C. *Geology*, *41*(8), 863–866. https://doi.org/10.1130/G34279.1

Verberne, B. A., Spiers, C. J., Niemeijer, A. R., De Bresser, J. H. P., De Winter, D. A. M., & Plümper, O. (2014). Frictional Properties and Microstructure of Calcite-Rich Fault Gouges Sheared at Sub-Seismic Sliding Velocities. *Pure and Applied Geophysics*, *171*(10), 2617–2640. https://doi.org/10.1007/s00024-013-0760-0

Yang, Y., Qiao, R., Wang, Y., & Sun, S. (2021). Swelling pressure of montmorillonite with multiple water layers at elevated temperatures and water pressures: A molecular dynamics study. *Applied Clay Science*, *201*, 105924. https://doi.org/10.1016/j.clay.2020.105924

Zhang, M. (2019). Stress-strain-sorption behaviour and permeability evolution in clay-rich rocks under CO2 storage conditions. *Utrecht Studies in Earth Sciences*, *188*. https://dspace.library.uu.nl/handle/1874/380664

Zhang, M., de Jong, S. M., Spiers, C. J., Busch, A., & Wentinck, H. M. (2018). Swelling stress development in confined smectite clays through exposure to CO2. *International Journal of Greenhouse Gas Control*, *74*, 49–61. https://doi.org/10.1016/j.ijggc.2018.04.014

Appendix A – Additional experimental measurements

Appendix A: Additional material properties and experimental procedure measurements.

Experiment number	Material	Sample holder	Pre-experimental Sample weight (gram)	Holds per SHS sequence (s)	Pre-experimental piston length (mm)	Final pioston length (mm)
u1196	OPA 1	2	0.72	a: 3 – 3000, b: 3 – 10000	-	203.20
u1198	OPA 1	2	0.79	a: 3 – 3000, b: 3 – 10000	-	203.20
u1200	OPA 2	2	0.81	a: 3 – 10000, b: 3 – 1000	204.22	203.40
u1202	OPA 3	2	0.92	a: 3 – 30000, b: 3 – 1000, 3 to 30000	203.63	-
u1203	OPA 3	3	0.75	a: 3 – 30000, b: 3 – 30000	204.40	203.00
u1205	SWy-2	2	0.85	a: 3 – 30000, b: 3 – 30000	-	201.83
u1206	OPA 3	1	0.51	a: 3 – 30000, b: 3 – 30000	203.78	-
u1210	SWy-2	1	0.59	a: 3 – 3000, b: 3 – 100000	203.38	202.40
u1211	SWy-2	2	0.88	a: 3 – 30000, b: 3 – 30000	204.10	201.92
u1212	SWy-2	1	0.58	a: 3 – 30000, b: 3 – 100000	203.33	202.25
u1217	SWy-2	1	0.56	a: 3 – 30000, b: 3 – 30000	203.46	201.80
u1218	SWy-2	2	0.88	a: 3 – 30000, b: 3 – 3000	203.77	203.30
u1221	SWy-2	2	0.88	a: 3 – 30000, b: 3 – 30000	203.85	202.40
u1222	SWy-2	2	0.89	a: 3 – 30000, b: 3 – 30000	203.80	202.30
u1223	SWy-2	2	0.89	a: 3 – 30000, b: 3 – 30000	203.81	202.05
u1224	SWy-2	2	0.90	a: 3 – 30000, b: 3 – 30000	203.80	202.40
dsOPA	OPA 3	-	3.2	a: 3 – 70470	-	-
dsSWy	SWy-2	-	4	a: 3 – 3000, b: 100 – 3000	-	-

Appendix B – TGA output curves

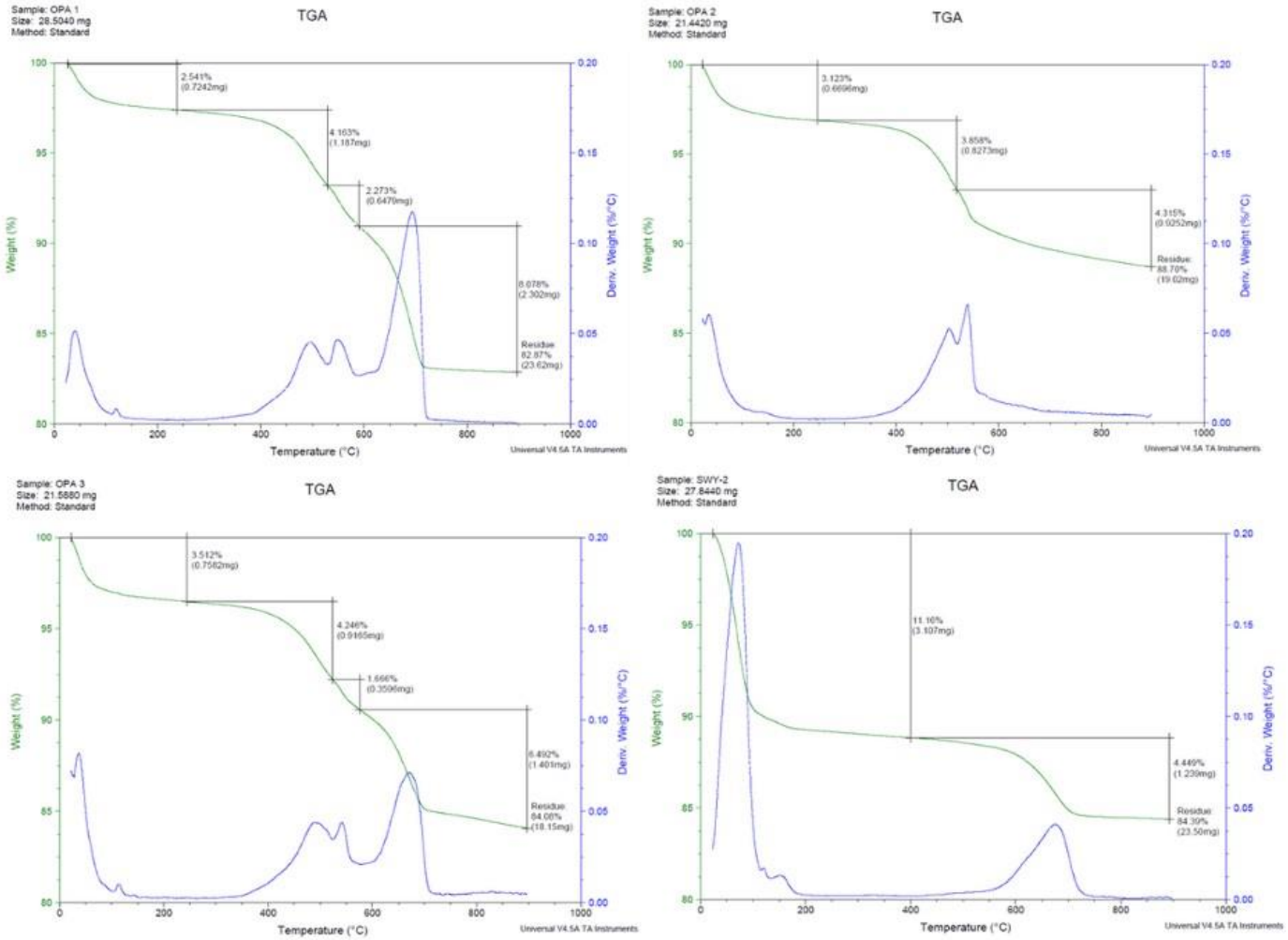

Appendix B: Results from the TGA measurements. Green curves show the weight loss as a function of the temperature increase and the blue lines, the rate of weight loss over the temperature. Sample material is indicated on the top left.